Systematic microstructure variability in double-diffusively stable coastal waters of nonuniform density gradient

Timothy F. Duda

Applied Ocean Physics and Engineering Department, Woods Hole Oceanographic Institution, Woods Hole, Massachusetts, USA

Chris R. Rehmann

Department of Civil and Environmental Engineering, University of Illinois at Urbana-Champaign, Urbana, Illinois, USA

[1] Conductivity microstructure, water velocity, and stratification were measured during a tow-yo transect near the New England shelf/slope front in early August 1997. Velocity data were collected with an acoustic Doppler profiler on the ship. The other data were collected with a towed platform. Estimates of χ, the rate of dissipation of temperature variance, were computed from the conductivity data with vertical resolution of 0.3 m. Relationships between χ and shear, temperature gradient, buoyancy frequency (N), and gradient Richardson number (Ri) were explored, with special focus on measurements taken in waters stable to double-diffusive processes (to avoid ambiguity of interpretation) and exhibiting variable density gradient (N ranging from 5 to 40 cph). For this subset of data, χ computed from data grouped into classes of local mean temperature gradient ($d\bar{T}/dz$) was proportional to $d\bar{T}/dz$ to the 0.7 power, which is consistent with diapycnal thermal eddy diffusivity K being proportional to $(d\bar{T}/dz)^{-1.3}$ within the framework of the Osborn-Cox model that relates χ and the mean temperature gradient to the heat flux. No correlation between K and Ri was observed, with Ri computed at 4 m vertical scale, so that systematic inhomogeneous large-scale forcing is not responsible for a false correlation of K and $d\bar{T}/dz$. Water mass salinity characteristics in the area caused N^2 to be proportional to $(d\bar{T}/dz)^{4/5}$, rather than to $d\bar{T}/dz$ as in the isohaline case, giving rise to the steep inverse relation $K = 10^{-10}N^{-3.3}$, with N in radians/s and diffusivity in m^2/s. The fit $K = 2 \times 10^{-9}N^{-2.5}$ results if one questionable data ensemble is disregarded. These relations are comparable to results obtained previously from the near-bottom tow data. They are not intended to be universal formulae but are meant to describe the conditions we encountered. They are not expected to hold at high and low values of N outside of our measurement range. An interpretation is that under these conditions the less strongly stratified (lower N) layers in this shelf area are more prone to instability of the larger-scale shear than the intervening interfaces, with the subsequent greater energy dissipation in the layers leading to higher buoyancy flux KN^2 in the layers than in the interfaces. *INDEX TERMS:* 4219 Oceanography: General: Continental shelf processes; 4524 Oceanography: Physical: Fine structure and microstructure; 4568 Oceanography: Physical: Turbulence, diffusion, and mixing processes; *KEYWORDS:* turbulent mixing, turbulent flux, diapycnal diffusion, eddy diffusivity, continental shelf waters, conductivity microstructure

1. Introduction

[2] The diapycnal fluxes of heat, salt, and other dissolved materials in coastal waters is influenced by many processes. Often, mixing processes and fluxes are considered within the framework of response to forcing, and are evaluated with respect to shear or shear stress. Here, we find that signatures of diapycnal mixing during stratified summer conditions vary in a measurable way with changes in an inherent property, local density gradient. In waters having density gradient varying an order of magnitude on scales of decimeters to meters, we find evidence that diapycnal eddy diffusivity and flux estimates intended to be valid for limited vertical layers (decimeters to meters vertical scale) are functions of the density gradient. Some possible causes and effects of density gradient–dependent flux such as we present here have already been discussed in the literature [*Balmforth et al.*, 1998; *Pelegrí and Sangrà*, 1998; *Phillips*, 1972; *Posmentier*, 1977].
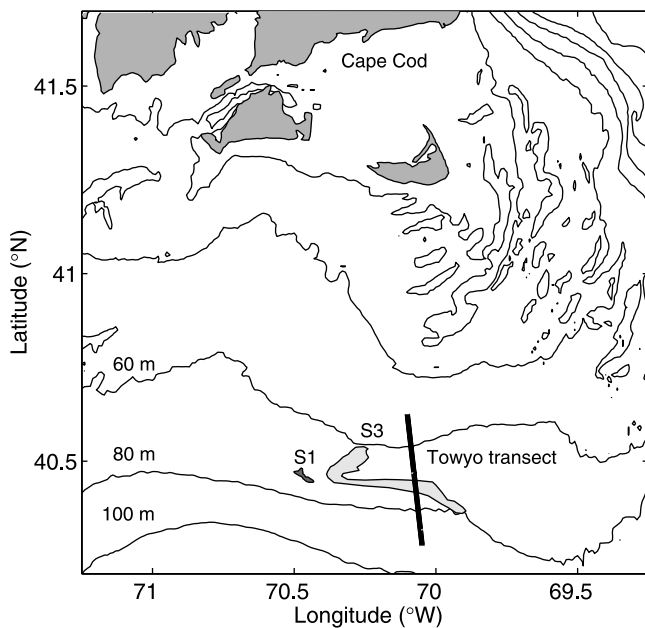
Figure 1. The experiment was conducted on the New England Shelf about 120 km south of Cape Cod. The data to be discussed were collected during a tow-yo transect shown by the line, which began about 3 hours after the third and final survey of an injected dye patch. The outlines of the patch during the first and third surveys are shown, marked S1 and S3. Bathymetry is indicated with contours at 20 m intervals.

[3] This work is distinct from studies of turbulent diapycnal diffusivity that have the goal of quantifying turbulent flux and comparing it to forcing functions at larger scales that can be resolved by numerical models. Understanding the response of flux to such forcing would allow parameterization of flux caused by subgrid scale processes in models. On the contrary, the results we obtain in this paper involve background density structures and turbulent flux residing entirely at the ordinarily subgrid scales of decimeters and meters, and most consequences, such as from flux convergence, for example, will be confined to those same small scales. This is not a limitation, however, because some biological and bio-optical processes or organisms appear to be sensitive to events and heterogeneities at these small scales. For example, narrow peaks in fluorescence have been observed in waters having vertically structured density gradient [cf. *Gardner et al.*, 2001, Figure 7; *Donaghay et al.*, 1992].

[4] Our data are from the Coastal Mixing and Optics (CMO) field program, which was sponsored by the U.S. Office of Naval Research and carried out by multiple investigators in September 1995 through August 1997. A goal of CMO was to understand mixing processes on the continental shelf south of New England, with emphasis on the stratified (nonwinter) period. We report on data collected during a 5.5 hour, 39 km tow-yo transect from south to north made during summer 1997 (Figure 1). Solar radiation warms the surface during the spring and summer and creates strong overall temperature and density gradients. The resulting thermocline erodes in the fall. The density structure

observed in our study was very steppy, with vertical density gradients varying by a factor of ten over scales of a few meters. The conclusion of our work, based on a modest amount of data, is that under these conditions the turbulent diapycnal diffusivity K depends strongly on local buoyancy frequency, i.e., K proportional to $N^{-2.9 \pm 0.4}$, so that the resulting buoyancy flux KN^2 is approximately inversely proportional to N. Such an inverse relationship between diapycnal flux and N would provide a positive feedback mechanism allowing the observed steppy fine structure to form and to persist.

[5] Our microstructure and supporting data were collected in August 1997 with a towed platform and an ADCP mounted on the tow vessel. Details of the observational program, the measurement system, methods of data collection, and methods of data reduction are described in a previous paper [*Rehmann and Duda*, 2000]. Our data show that microstructure, shear, and stratification are variable processes, consistent with previous work, and we investigate relationships between microscale signals and both the shear and stratification. Many of the relationships involve estimates of K, which are derived from the thermal variance dissipation rate χ via the Osborn-Cox (OC) model [*Osborn and Cox*, 1972], where $\chi = 2D_T(\nabla T')^2$ and where D_T is the molecular heat diffusivity. The overbar indicates average. The only relationship that emerges with reliability is the above-stated relation between K and N, with each quantity computed over five independent ensembles of data assembled from physically scattered locations, with ensembles distinguished by local $d\bar{T}/dz$ of the individual members, where $d\bar{T}/dz$ is the temperature gradient after filtering out microstructure with wavelengths below 20 cm.

[6] Three types of stable stratification were encountered during CMO: Water stable to double diffusive processes (double-diffusively stable, DDS), where cool salty water underlies warmer fresher water; water conducive to the formation of salt fingers (SF), where cool fresh water underlies warm salty water; and water conducive to the double-diffusive layering (DDL) instability, where warm salty water underlies cooler fresher water [see, e.g., *Turner*, 1973]. The final analyses of this paper use only data from DDS conditions in order to strengthen the interpretation. The inclusion of data from the other conditions would complicate our interpretation because of the possibility of intermingled microstructure and flux from two processes, shear-generated turbulence and double-diffusive instability.

[7] The major result of our previously published paper [*Rehmann and Duda*, 2000] was a trend toward reduced diffusivity K at increased buoyancy frequency N. However, Rehmann and Duda found that a single relationship between K and N cannot describe the entire water column. Detailed near-bottom measurements gave a different result than measurements taken well away from the bottom. The relation $K \propto N^{-3.1}$ was observed under DDL conditions within and just above a warm salty bottom layer, of thickness about 5 m, using horizontal tows. On the other hand, the relation $K \propto N^{-1.3 \pm 0.8}$ was observed in data collected well above the bottom, from all conditions (DDS, SF, and DDL), during the transect we report on here (Figure 1), with a steeper relation suggested for a subset of transect collected under DDS conditions. It should be noted that the $N^{-1.3}$ fit

for the transect was less convincing than the $N^{-3.1}$ fit, with large residuals, motivating this more detailed study.

[8] The near-bottom results of *Rehmann and Duda* [2000] form a baseline for this study because they are derived from a more homogeneous and more simply analyzed data set than the transect provides, and because they have a good power law fit, so they are summarized now. Eleven towed sampling runs were made at depths ranging from 1 to 10 m above the bottom in a relatively confined area. A warm salty layer was separated from colder fresher water above by a sharp interface (the foot of the shelf break front, actually) typically found 6 m above the bottom, with maximum temperature gradient of 0.5°C/m and N of about 30 cph (0.05 rad/s). The stratification was strongly depth dependent, with N ranging from a few cph very close to the bottom to the 30 cph of the interface. The OC relation $K = 0.5 \, \chi \, (\partial \bar{T}/\partial z)^{-2}$ was employed in each layer (see section 4). The relationship $K = 2.1 \times 10^{-10} N^{-3.1}$, with N given in rad/s and K in m²/s, emerged after the procedure of computing K from mean χ and $d\bar{T}/dz$ within layers, each with a known N.

[9] The near-bottom relation ($K \propto N^{-3.1}$) was reliably measured because of the large quantity of data collected under comparable conditions. Microstructure was examined as a function of density, and density was directly associated with stratification because conditions were temporally stable, enabling a direct comparison of microstructure and K to N. On the contrary, the tow-yo data were collected in continually changing conditions, so comparison of K and N requires different analysis procedures.

[10] To determine the reliability and the meaning (if any) of the quoted midwater $K \propto N^{-1.3}$ relation, we perform some further analyses in this paper. First, the published transect K versus N comparisons are presented again, although in a slightly modified form. Next, we investigate K with respect to gradient Richardson number ($Ri = N^2/U_z^2$, where U_z is vertical shear of horizontal velocity) by merging shipboard ADCP velocity data with tow vehicle density data. No dependence of K on Ri emerges. Perhaps more importantly, the higher K values at low N are not found to be associated with lower Ri. Such an association, if observed, would have created an alternative explanation of the apparent K versus N result. To proceed further, a selected subset of data is investigated. This subset is composed of data taken at depths where we can produce denoised velocity data, where ADCP profiles and tow-yo data match in time, and where the stratification is of the DDS type. This is about fifteen percent of the data used in the K analysis of the previous paper. The results for this subset of data do not provide additional insight: No clear relation is seen between K and Ri, and K varies strongly with N. Since no Ri dependence is seen, an enlarged set composed of good microstructure data from DDS water, including those without reliable Ri estimates, are examined in order to verify the K to N relation by reducing the confidence intervals. This final examination yields our primary result, $K \propto N^{-2.9 \pm 0.4}$.

[11] This power law relation is close to that obtained from the near-bottom data and fits much better than the high-residual $K \propto N^{-1.3}$ relation. The high residuals may have resulted from nonhomogeneous forcing conditions since some of the data analyzed in the previous paper were from double diffusively unstable water near the front in the southern end of the transect. There is no evidence of a relationship between K and Ri in any of our analyses. Such a relation between mixing and forcing is sometimes used in numerical models [*Mellor and Yamada*, 1982; *Pacanowski and Philander*, 1981], but Ri is difficult to measure in unsteady oceanic flow from a moving ship, and delay between shear and turbulence in unsteady flow would make such a relationship difficult or impossible to measure, except possibly with Lagrangian methods. The issue of the role played by the temporal relationship between turbulent diffusion and previous fine structure in the development of pycnocline structure has recently been resurrected by *Pelegrí and Sangrà*, [1998] and *Smyth et al.*, [2001] contains an up-to-date discussion of time-dependent behavior in turbulent patches.

[12] The paper is organized as follows. Section 2 describes our instrumentation and some of our data reduction procedures. Section 3 shows conditions in the transect, such as currents and water masses. Section 4 shows the K vs. N relationship of the previous paper and a K vs. Ri relationship computed in a consistent manner. Section 5 describes and shows the results of detailed reanalysis of the DDS subset of the transect data. Section 6, preceding the conclusion, discusses the possible causes and the implications of the observed relationship between K and N, and shows results from numerically simulated diffusion through a fluid with N-dependent K.

2. Instruments and Data Collection

[13] The measurements were made in conjunction with dye injection studies of diapycnal diffusion. Dye studies were undertaken in summer 1995, 1996 and 1997. Our intention was to measure stratification, fine-scale shear, and scalar microstructure during surveys of the dye patches to investigate the characteristics of the turbulent patches presumed to be responsible for dye dispersal. A microscale conductivity probe was fitted to the fast moving dye measurement tow platform (2 to 2.3 m/s) to measure temperature microstructure. However, electrical noise from the dye-sensing fluorometer severely restricted the utility of the conductivity probe during dye surveys. The problem occurred only when the entire system was immersed in seawater and may have been due to electromagnetic fields in the water induced by varying currents to the fluorometer, which flashed its lamp and recharged at the rate of 5.5 Hz. Because of the problem we do not have concurrent dye and microstructure measurements. However, we were able to obtain usable microscale conductivity data with the fluorometer turned off, allowing collection of the data shown here.

[14] The instrumentation suite is fully described by *Rehmann and Duda* [2000]. Briefly, a 200 kg platform was towed behind the RV *Oceanus*, with data transmitted up the electrical/mechanical cable. Conductivity microstructure was measured with a Sea-Bird Electronics SBE 7 sensor mounted at the bow of the platform. Other instruments were a Sea-Bird 9+ CTD, two Chelsea fluorometers, an Ocean Sensors OS200 CTD, a Marsh-McBirney current meter, a Datasonics (now Benthos) altimeter, and a Precision Navigation TCM2 three-axis attitude sensor. Two Sea-Bird C/T

sensor pairs provided redundant measurements of the temperature (T) and salinity (S) fine structure at 6 Hz, giving "background" $\bar{T}$ and $\bar{S}$. The fluorometers measured dye concentration and chlorophyll for the tracer dispersion study.

[15] The ADCP was an RD Instruments 300 kHz vessel mounted broadband unit, with the transducer at 5.7 m depth in the *Oceanus* well. Three-axis attitude sensing was not successfully implemented into the ADCP system. ADCP depth binning was set at 2 m. The instrument averaged pings for 45 seconds. The data were later smoothed, and outlier data caused by bad bottom tracking were removed, providing profiles each 135 s. Shear is computed in two ways in this paper: Center difference of vertically unfiltered velocity profiles, and first difference of EOF mode-filtered profiles (Appendix A). These processes resolve shear from signals greater than at 8 m and 4 m wavelength, respectively. Shear from wavelengths approaching these is not fully resolved; there is attenuation which depends on the spectrum in the manner described by *Gregg and Sanford* [1988], which is probably about a factor of two, but isn't known. Shear is not adjusted upward to accommodate for this. Ri and Ri^{-1} estimates are made using appropriately filtered density profiles and have the same resolution as the shear profiles used in their computation.

[16] The tow platform was designed to move smoothly through the water with low attack angle. A tail with fins stabilized the flow direction at the nose and thereby limited any attack angle fluctuations induced by ship heave and pitch. The platform achieved low angle of attack while being winched in (tow-yo up casts) or towed level, but did not perform well when the cable was payed out. For this reason we do not include data collected during cable payout (descent).

[17] The SBE 7 sensor had two forward directed platinized electrodes. A comparable sensor is described by *Meagher et al.* [1982]. The sensor output is preemphasized to increase signal-to-noise ratio at high frequencies. The output was filtered with a fourth-order, 120 Hz low-pass Butterworth filter to reduce aliasing, sampled at 400 Hz, synchronized with data from the other instruments, and transmitted up the tow cable to the ship. The dynamic range of the filter and the A/D system circuitry was 90.7 dB. With the probe in air (i.e., zero conductivity gradient) the range was reduced to 77.4 dB, with a system output (noise) of 2.7 mV RMS. The minimum measurable χ for this system in conditions of uniform salinity is 2×10^{-10} K^2 s^{-1}.

[18] Estimates of χ were derived from conductivity gradient variance using the white spectrum algorithm of *Washburn et al.* [1996]. Conductivity gradient variance (CGV) was obtained within 1 s windows by integrating the one-dimensional along-track conductivity gradient spectrum $S_C(k)$. The 1 s windows typically extended 2 m horizontally and were typically less than 0.3 m vertically. The vertical extent was controlled by the winch speed (usually 0.25 m/s) and ship motion. A 400 point Hanning taper was used in the spectral computation. After the preemphasis and the antialias filter responses were accounted for, S_C was integrated and CGV was computed assuming the small-scale field to be isotropic. More detail about the application of the *Washburn et al.* [1996] algorithms are given by *Rehmann and Duda* [2000] and section
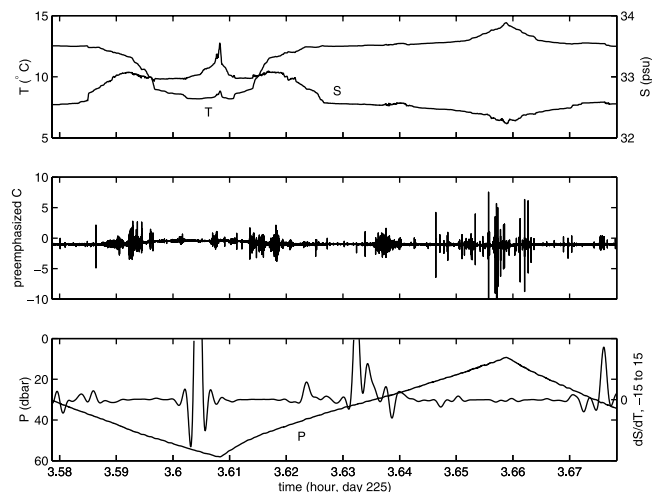
Figure 2. Example of a 6 min segment of data measured during the tow-yo transect: (top) T and S from the SBE-9+ CTD. (middle) Unprocessed, preemphasized microscale conductivity signal, essentially the conductivity gradient plus the conductivity. Quiet (low gradient) sections are punctuated by patches of microstructure. (bottom) Pressure, P, and $d\bar{S}/d\bar{T}$. Except for the the DDL conditions seen at the bottom, the data show the DDS conditions that prevail in much of the transect.

5 of this paper. Figure 2 shows $\bar{T}$, $\bar{S}$, microscale conductivity, P (platform pressure) and $d\bar{S}/d\bar{T}$ for one 6 min segment of the transect.

[19] Two factors determine the sign and magnitude of salinity contributions to the conductivity: The correlation between T and S, and the slope of the TS relation ($d\bar{S}/d\bar{T}$). The TS correlation determines the contribution of the cross spectrum of T and S to the conductivity spectrum, the other term relates the relative strengths of temperature and salinity contributions to conductivity variations. In addition, our scientific analysis requires $d\bar{T}/dz$. For each χ estimate from the transect, accompanying $d\bar{S}/d\bar{T}$ and $d\bar{T}/dz$ estimates were derived from lines fitted in the least squares sense to the six $\bar{S}$, $\bar{T}$ and low-pass-filtered P measurements collected in the 1 s window (approx 2 m of path). Only data from periods when the r^2 value of this fit exceeded 0.5 were accepted for analysis, so that only a subset of data collected during ascent (and none during descent) were analyzed. Salinity spiking from T and S probe mismatch does not affect the $d\bar{T}/dz$ estimates and only rarely affects the $d\bar{S}/d\bar{T}$ values. $d\bar{T}/dz$ is required in the Osborn-Cox model, and it plays a prominent role in determining an N-dependent K.

3. Conditions Encountered in the Transect

[20] Environmental conditions such as currents and large-scale (4 m) Richardson number patterns do not enter into our statistical K versus N analysis in forthcoming sections. They are nonetheless presented here for completeness in the documentation of our study.

[21] The transect was made just after the second of two dye injection mixing experiments. The dye was injected on 7 August 1997 at 40° 30′ N and 70° 30′ W into the center of
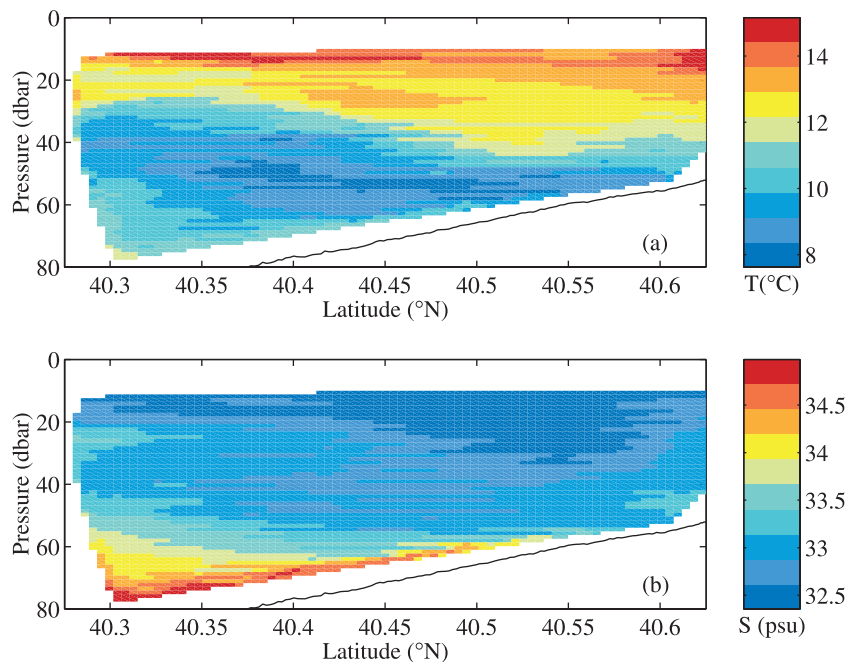
Figure 3. Temperature and salinity of the transect are shown. The line shows the seafloor depth. The boundary between the near-bottom warm salty water and the water above is a portion of the shelf/slope water front, which extends to the surface to the south of the transect, in deeper water (i.e., to the left).

a DDL interface separating warm salty water from the overlying cooler fresher coastal water, typically 5 m above the bottom (Figure 3). The dye patch was surveyed and mapped three times. The outlines of the patch during the first survey (taken between 1 and 15 hours after injection) and the third survey (95 to 125 hours after injection) are shown in Figure 1. The transect started 128 hours after injection and took 5.5 hours. The third survey revealed that the dye patch had drifted to the east and had split into two lobes. The northwest lobe was in the warm salty bottom

layer and was moving up the slope, in contact with the bottom at the extreme northern edge. The southeast lobe, not in contact with the seafloor, had moved upward a few meters and the extreme southern edge had moved into deeper water. The vast majority of the dye was in the western portion of the southeast lobe, at 40.45 N and 70.2 W in Figure 1. Estimates of K from dye dispersal and microstructure measurements at the dye density were found to compare well, both fluctuating around 5×10^{-6} m^2/s [*Rehmann and Duda*, 2000].
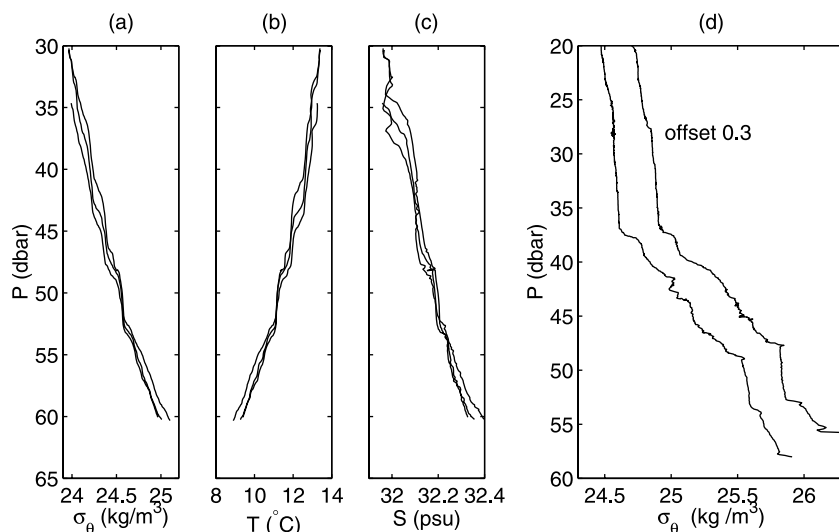
Figure 4. Carefully processed (a) density, (b) temperature, and (c) salinity from three consecutive dye study tow-yo profiles: 1996b-3-761 to 763. The isopycnals move upward over time during the 150 s record. (d) Density profiles computed from unprocessed Seabird 9+ data recorded during two consecutive upward casts of our transect.
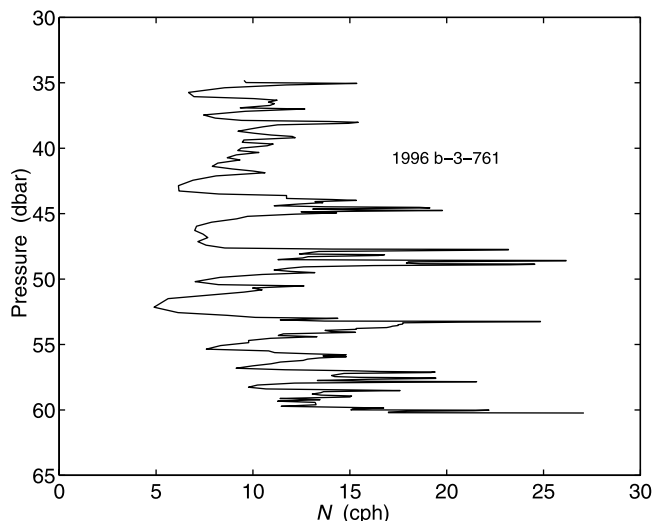
Figure 5. N is shown for CMO dye study profile number 1996b-3-761 of Figure 4.

[22] DDS conditions prevailed above and to the north of the dye in fresh shelf water warmed by the summer sun. Density profiles in this water mass exhibited detailed fine structure. Figure 4 shows three consecutive density profiles from this water mass, taken at 50 s intervals at tow speed 2 m/s. Although they were measured the year before, these profiles are examples of our most accurate density measurements. They are produced by carefully processing the Sea-bird 9+ temperature and conductivity data to minimize density mismatch of consecutive profiles. The density profiles are given as pressures of equally spaced density values at interval $\delta\sigma_\theta = 0.005$, and N is computed using the pressure difference and $\delta\sigma_\theta$, with no smoothing. The procedure resolves detailed vertical structures. The resulting profiles have density inversions in only 0.2 percent of the record, suggesting very little mixing, or at least, suggesting overturn scales too small to sample with the 9+ CTD operating at 6 Hz. In the same figure are two density profiles measured during our transect with the same 6 Hz instrument, but not processed in any way. These show the same highly variable vertical density gradients as the carefully processed profiles.

[23] Figure 5 shows N computed directly from the first 1996 profile shown in Figure 4, with values ranging from 4 to 27 cph, which means that N^2 (density gradient) varies by a factor of fifty. Profiles by J. A. MacKinnon and M. C. Gregg (Mixing on the late summer New England shelf: Solibores, shear, and stratification, submitted to *Journal of Geophysical Research*, 2001, hereinafter referred to as MacKinnon and Gregg, submitted manuscript, 2001) taken in late summer 1996 in the area also show a factor of 100 variability in N^2. The variance is another way to quantify the N variability: One hundred profiles (numbers 761 to 860) covering 30 to 66 m depth from the second dye study of 1996 had variance 44 cph^2 (rms N variation of 6.6 cph).

[24] The currents in the area were measured with the dye and the ADCP. The dye clearly moved to the east (Figure 1). Currents measured during the transect are plotted in Figure 6. A tidal current estimate has been removed. The
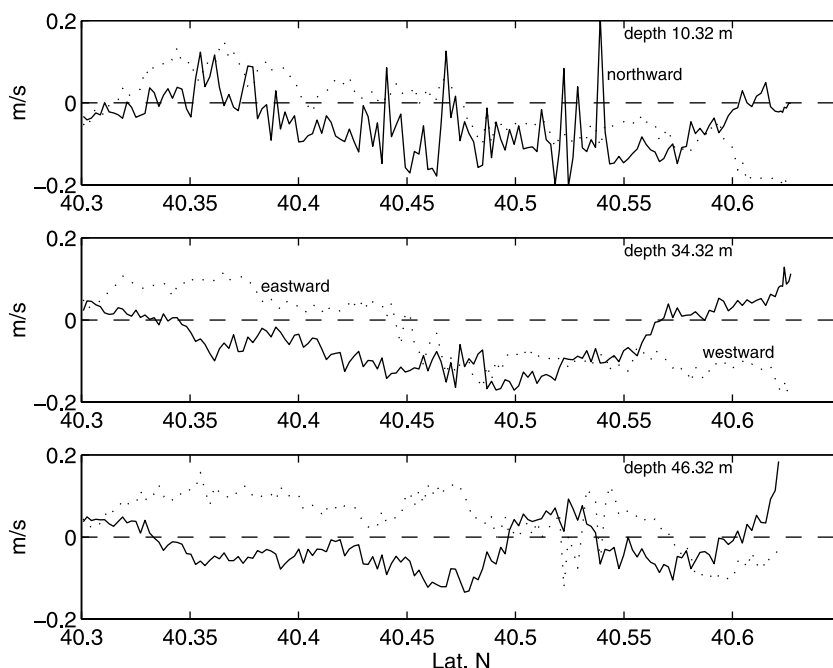
Figure 6. Eastward (dotted line) and northward (solid line) velocity components measured during the transect are shown for three depths: (top) 10 m, (middle) 34 m, and (bottom) 46 m. The northward spikes at 10 m depth between 40.50° and 40.55° N, and perhaps others, are currents of solitary waves moving to the north. The mean currents are eastward south of 40.40° N. Between 40.4° and 40.5° N the upper currents rotate to become westward at 40.5° N. Between 40.50° and 40.55° N, there is a large shear between 34 and 46 m that is evident in Figure 8.
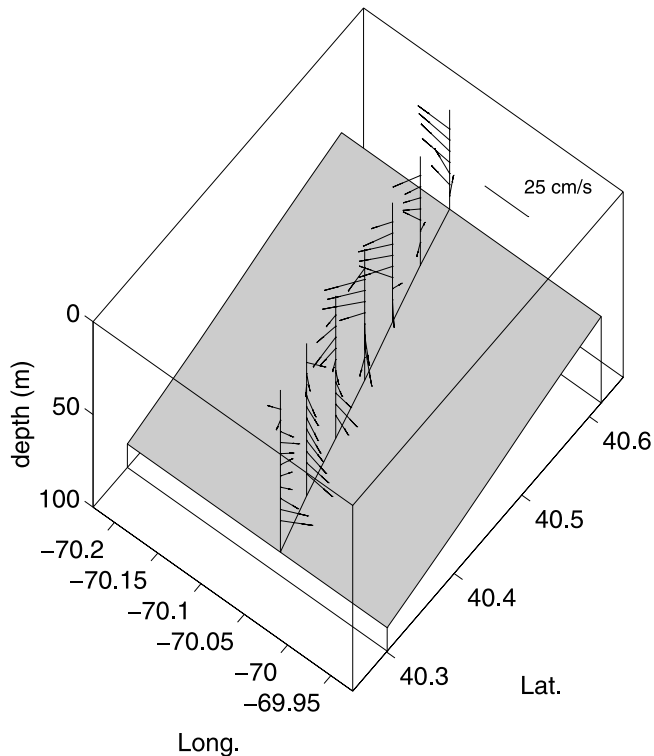
Figure 7. Detided velocity within the transect is shown by vectors directed outward from the vertical bars. A vector of length 0.05° indicates a current of 25 cm/s, as shown. The current magnitudes are typical for summer in this area.

estimate is from *Moody et al.* [1984] and is derived from a 61 m record near our injection location (their Station P), and it fits the depth-averaged currents well. Figure 7 shows current vectors. At the offshore end of the transect the currents tend to be eastward (from the west). Moving north along the transect, the surface currents "veer" to become southward (from the north) and continue veering to become westward. The deeper currents are also eastward at the offshore end, veering slowly to become southeastward (at 40.5° N and 34 m depth in Figure 6, for example), and finally diminishing at the northern end of the transect. Winds were 3–5 m/s at the time. Waves and swell were 0.5–1.5 m.

[25] Shear and N^2 within the transect exhibited some notable structure. They did not appear to be purely stochastic variables. Both parameters were computed for depths between 10 m below the surface and 10 m above bottom and are shown in Figure 8. N^2 was quite low at depths of 20 to 30 or 35 m between 40.45° N and 40.57° N, shown by the blue color and the well-spaced isopycnals. Below this weakly stratified region there are laterally coherent bands of variable but low N^2. At roughly 12 m above the bottom a strongly stratified interface separates the underlying warm salty slope water from the shelf water. Near the surface, a high-N layer can be seen south of 40.45° N. Shear was above its typically low level in two places: a "layer" sloping downward to the north, north of 40.45° N, and isolated locations at depths between 15 and 20 m. The latter, the strong near-surface shears, are due to waves, probably packets of internal solitary waves. The high-shear event at

40.525° N corresponds to a 10 m displacement of the thermocline. (The displacements of individual waves in a packet are not resolved by the tow-yo). Note that the observed flow variability in the transect may not be spatial, but instead due to temporally evolving baroclinic tidal or inertial flows.

[26] N^2 and U_z^2 in the figure can be combined to form Ri^{-1} (Figure 9). High Ri^{-1}, consistent with an increased tendency for shear instability, is found in patches within the deep high-shear layer and in some, but not all, of the surface high-shear events. The shear shown in the figures is computed by center differencing the velocity profiles; no attempt beyond temporal averaging and outlier removal has been made to reduce the effect of ADCP measurement noise in these figures.

4. *K* Versus *N* and *Ri* for All Stratification Classes

[27] These CMO transect data were examined using the Osborn-Cox (OC) model by *Rehmann and Duda* [2000], and we wish to revisit, explain, and diagnose their results in this section. The OC model can be applied to ensembles of data to obtain *K*, provided that conditions are stationary, that each ensemble can provide meaningful estimates of mean temperature gradient and mean χ, and that the other conditions required for the model to be valid are met. *Washburn* [1987] has demonstrated that the OC conditions are met in a spatial volume of one coastal data set. The model is valid when two terms of the simplified budget equation for temperature variance dominate, the production and dissipation terms. That equation is

$$\frac{\partial \overline{(T')^2}}{\partial t} = \frac{-\partial \overline{u_i (T')^2}}{\partial x_i} - 2\overline{u_i T'}\frac{\partial \bar{T}}{\partial x_i} - \chi \qquad (1)$$

If the time derivative and divergence terms can be neglected, and if an eddy diffusivity *K* relates flux to mean gradient, the OC relation holds, $K = \chi/2(d\bar{T}/dz)^2$.

[28] *Rehmann and Duda* [2000] created ensembles by separating data according to stratification classes (DDS, DDL, SF) and further separating them by *N* in each class, giving 24 ensembles. *K* for each ensemble is plotted versus *N* by *Rehmann and Duda* [2000, Figure 20], with *K* computed in each ensemble using mean χ and mean $d\bar{T}/dz$ of the ensemble. This procedure is valid if this grouping of the data does not invalidate the OC model assumptions which have been presumed to hold over long periods for specific volumes of water [cf. *Davis*, 1994]. The OC model will remain valid for the grouped and averaged data if the following terms are negligible: The average flux divergence of the data volumes included in each ensemble, the mean rate of change of temperature variance $\overline{(T')^2}$ for those volumes, and cross terms. We have not measured these terms. They are difficult if not impossible to measure in the field. On the other hand, no mechanism has been offered to enable $(\partial/\partial x_i)\overline{(u_i (T')^2)}$ to reach a magnitude comparable to the production and dissipation terms at the spatial scales we are considering. This term is discussed in Appendix B. Our procedure of computing averages after partitioning data into parameter regimes (*N* and class in this case) rather than over time or space is not unprecedented. For example, *St. Laurent and Schmitt* [1999]
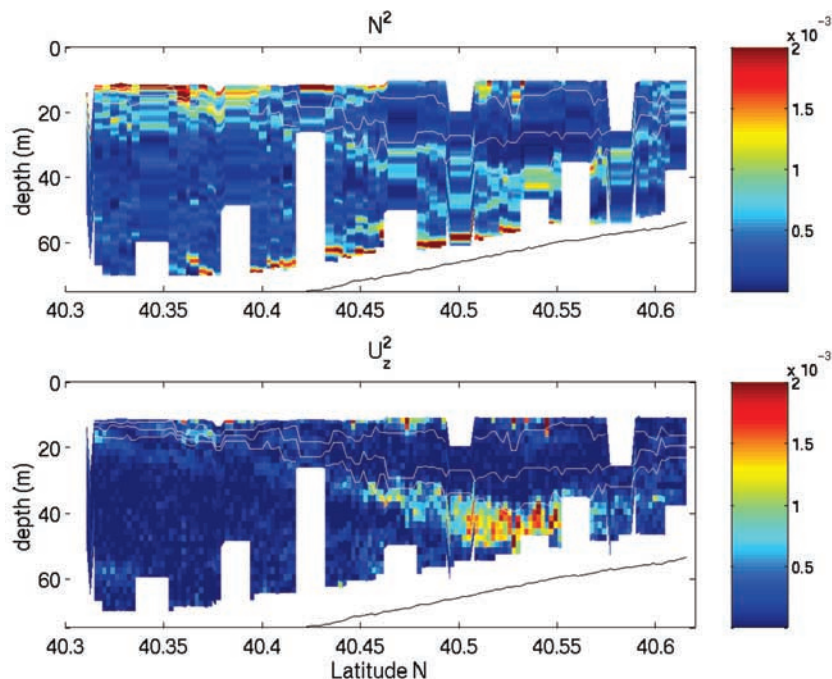
Figure 8. Buoyancy frequency and shear squared plotted for the tow-yo transect. The white stripes show areas of horizontal towing (restricted vertical coverage). Three isopycnals are shown: 1024.365, 1024.565, and 1024.765 kg m^{-3}.

have recently partitioned data into Ri and density ratio classes and then applied the OC and other models.

[29] *Rehmann and Duda* [2000] state that the results from the 24 ensembles suggest K proportional to $N^{-1.3\pm0.8}$ for all three stratification types. They do not discuss this result in detail so it is reproduced here in modified form. This new

analysis is slightly different because we wish to include Ri^{-1} to investigate whether variable shear or Ri^{-1} caused any of the variability in K, giving an alternative explanation of the apparent relationship between K and N. This requires an additional computation of mean Ri^{-1} for each ensemble of points, with the points of each ensemble taken from
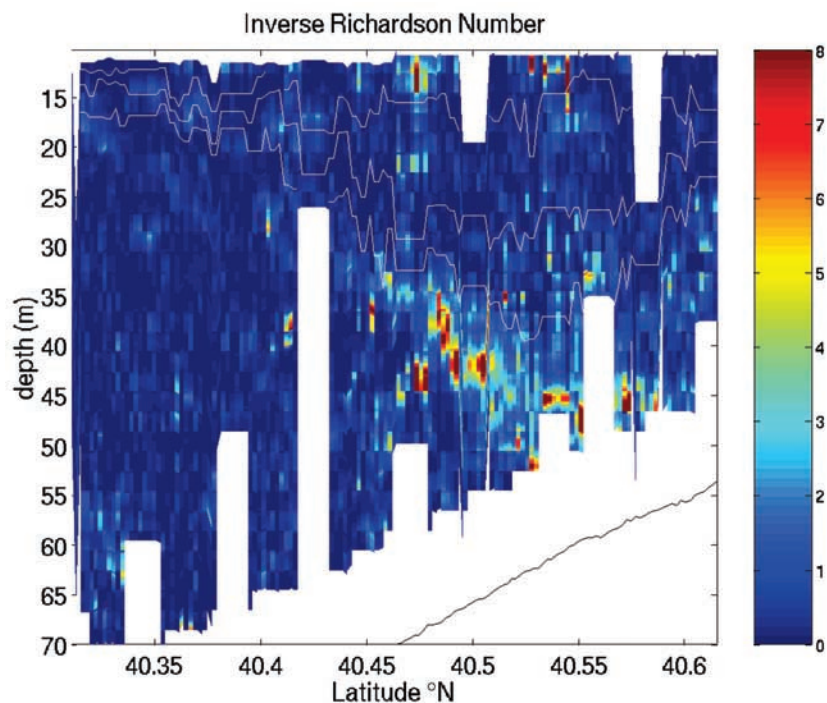
Figure 9. Inverse Richardson number computed from the data of Figure 8.
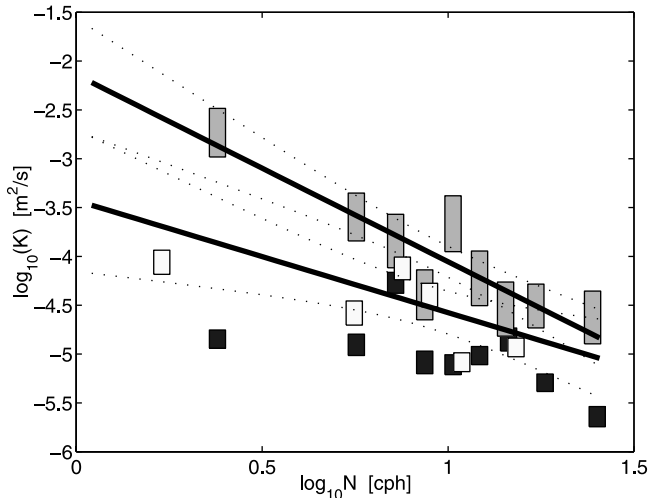
Figure 10. Results of analysis very similar to that quoted by *Rehmann and Duda* [2000] are shown. The boxes show the K versus N for independent groups of transect data. Microstructure data are separated according to both stratification type and N. The shaded, white, and black boxes show results for DDS, SF, and DDL stratification, respectively. The height of the boxes indicate upper and lower bounds on K, computed from mean upper bounds and mean lower bounds of χ within the bins, respectively. The lower solid line is a K versus N power law fit to all data shown. The fit is K proportional to $N^{-1.1}$, similar to that quoted by *Rehmann and Duda*, [2000] for these transect data. The upper solid line shows the K versus N power law fit for DDS points only, with $K \propto N^{-1.9}$. The dotted lines show 95% confidence bounds for the two fitted lines.

widely scattered depths and times, but shear and Ri^{-1} are not available for all of the points used by *Rehmann and Duda* [2000], so the analysis here uses only a subset of those points. The inverse of the Richardson number is used because near-zero shear is encountered more often than near-zero stratification, making Ri^{-1} better behaved than Ri.

[30] The ADCP data and tow-yo data are not synchronized and must be merged to obtain Ri^{-1}. Despiked, corrected velocity profiles are obtained each 135 seconds (270 m of ship track). The ADCP data and the towed platform data were merged using the following procedure: If the midpoint time of the ADCP sampling interval, with 30 seconds s subtracted from it to account for a 60 m distance between the ship and the tow platform, is within 30 s of the microstructure and density record from the tow platform, then the ADCP data and the tow sled data are merged and retained for analysis. Otherwise, the data are not considered. Roughly one-half the data points in each original ensemble of *Rehmann and Duda* [2000] are eliminated by this procedure, and we form a new group of ensembles with the retained points. Inverse Ri has been obtained for the remaining points, computed with center difference ADCP shear ($U_z^2 = (dU/dz)^2 + (dV/dz)^2$) and 4 m low-pass-filtered N, to match resolution scales.

[31] Figure 10 shows K versus N for the resulting ensembles. A power law fit between K and all N gives the lower line, K proportional to $N^{-1.15}$. The fit is a linear

regression between the logarithms of K and N. 95% confidence intervals are shown. The r^2 value of the fit is 0.29. The data show reduced K for SF and DL water types, mostly associated with the near-bottom layer and the shelf/slope water front, areas mostly offshore and/or below the main DDS water mass. To eliminate the effects of the DL and SF areas, a second regression was performed for DDS points only, shown by the upper line. The result is $K \propto N^{-1.9}$, with $r^2 = 0.85$.

[32] Figure 11 shows K versus mean Ri^{-1} for the same 24 new ensembles, with a fitted curve and 95% confidence bounds. The plotted line is a least squares linear fit between $\log K$ and $\log$ mean Ri^{-1}. No relationship can be established between K and Ri^{-1} based on the family of widely varying lines fitting within the dotted confidence bounds. The r^2 value of the fit is 0.01. A notable feature is that the high K value does not occur at high Ri^{-1}, a simple expectation for shear-driven turbulent diapycnal mixing. This means that anomalously high Ri^{-1} does not offer an explanation of the high K point at low N. Another feature is that K has different behavior versus N and versus Ri^{-1} for the three classes, and we offer no explanation beyond a perhaps obvious appeal to inhomogeneous forcing, difficult to detect with our poorly resolved Ri^{-1} measure, acting on different classes. Also, the DDL and SF measurements come often, but not always, from the vicinity of the shelf/slope water front, whereas the others come mostly from north of the front.

5. Improved K Versus N: Double-Diffusively Stable Conditions

[33] The DDS data of the previous section show a fairly consistent K to N relationship. However, the large number of N bins (nine), the reduction of data quantity caused by requiring a colocated reliable Ri value, and the preliminary method of computing χ from conductivity gradient variance in DDS waters result in large confidence intervals of the K values. More rigorous analyses of the DDS data set are performed in this section to better constrain the K versus N relationship. Furthermore, estimates of shear are improved using complex empirical orthogonal function (EOF) filtered versions of the ADCP record, Appendix A. The results suggest that χ is related systematically to $d\bar{T}/dz$, i.e., $K \propto (d\bar{T}/dz)^{0.7}$. Application of the OC model then gives K proportional to $(d\bar{T}/dz)^{-1.3}$. Local water mass characteristics create a TS relation such that $N^2 \propto (d\bar{T}/dz)^{4/5}$, leading to a steeper inverse relation $K \propto N^{-3.3}$ than would be the case for uniform salinity water ($K \propto N^{-2.6}$). A second relation, $K \propto N^{-2.5}$, results when one of five data ensembles is disregarded. As in the previous section, no K to Ri relation can be determined, with Ri computed at roughly the 4 m scale. Data processing procedures are explained first, and then results are shown.

5.1. Computing χ

[34] Dissipation rate (χ) values are obtained from microscale conductivity using a slightly different method than that used in the previous paper, and by corollary in the previous section. As in the previous analyses, χ is derived from conductivity gradient variance within 1 s time windows. Unlike those analyses, we use only the lower of two χ estimates available from the algorithms of *Washburn et*
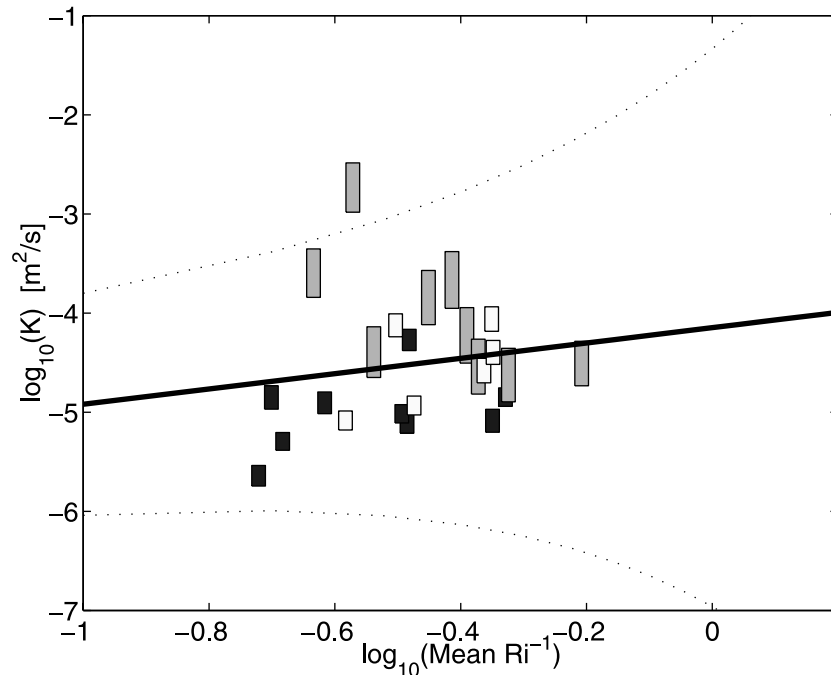
Figure 11. Dependence of mean K on mean Ri in the transect using analyses of *Rehmann and Duda* [2000]. The data are divided into the same groups as for the analysis shown in Figure 10. The color indicates DDS, SF, and DDL samples as in Figure 10. Ri^{-1} is computed using centered difference shear and N filtered to match the shear scale. The K values are those of Figure 10. The line shows the least squares power law fit. The 95% confidence bounds (dotted lines) of the fit show that even the sign of the power law is indeterminate.

al. [1996]. Two values were shown earlier (the upper and lower edges of the symbols in Figures 10 and 11), referred to as upper and lower bounds on χ, but here we dispense with the higher values. The decision to use only the lower estimate in DDS conditions can be understood by considering the nature of the correction algorithms. The essence of those algorithms is to compute the theoretical ratio of the integral of observed, probe response limited conductivity gradient spectrum (the observed variance) to the true temperature gradient variance, with the aid of auxiliary measured characteristics, primarily local $d\bar{S}/d\bar{T}$. An estimate of the true temperature gradient variance (proportional to χ) is obtained by dividing the observed conductivity gradient variance by the theoretical ratio, which is generally greater than one.

[35] Since the SBE 7 sensor resolves virtually all temperature microstructure except at extremely high dissipation rates, the correction procedure subtracts signal (associated with the salinity spectrum and the temperature-salinity cross spectrum) rather than adds it, unlike inverse filtering procedures generally applied to slowly responding thermal probes. One unknown remains in the correction procedure: the T to S coherence near the Batchelor scale of temperature roll-off, which has never been measured and remains a challenge. (*Nash and Moum* [1999] measured T and S at dissipation scales and discuss this term). In DDS conditions, i.e., $d\bar{S}/d\bar{T} < 0$, perfect correlation between T and S near the Batchelor scale of temperature roll-off would imply a smaller observed conductivity variance than would no correlation. This is because the observed conductivity spectrum would contain a null at the Batchelor scale if T

and S remain negatively correlated, a null which we do not generally observe in our records. The null will not exist if differing effects of thermal and haline diffusion acting on gradients at the Batchelor scale destroy the dS/dT of larger scales, giving no T and S correlation. We adopt the convention of no correlation, which is equivalent to choosing what *Rehmann and Duda* [2000] refer to as the "χ lower bound" to be the best estimate of χ in DDS conditions.

5.2. Results

[36] Figure 12 shows χ plotted against $d\bar{T}/dz$ and Ri^{-1}. All variables are computed for 1 s data segments. The temporal matching procedure of section 4 is used to obtain Ri^{-1} from the EOF-filtered velocity and tow sled data, rather than an interpolation scheme. An unreliable but suggestive line fits χ versus $d\bar{T}/dz$. This line is consistent with an inverse relationship between K and $d\bar{T}/dz$ because K is proportional to $\chi \, (d\bar{T}/dz)^{-2}$. There is no apparent dependence between χ and Ri^{-1}. The procedure of fitting χ to $d\bar{T}/dz$ is inconsistent with the OC model, however, since the averaging included in the model formulation is not performed. Therefore, the relationship of χ to temperature gradient suggests that mixing may depend on temperature gradient, but the dependence can not be interpreted in terms of the OC model. Analyses that are consistent with OC need to be done. The approach we adopt is ensemble averaging that is similar to the N-averaging of section 4.

[37] A simple way to test for a three-parameter relationship of K to N and Ri is to bin the data by both N and Ri and then compute mean χ, mean $d\bar{T}/dz$ and K for each ensemble. This procedure was followed for three N and three Ri^{-1}
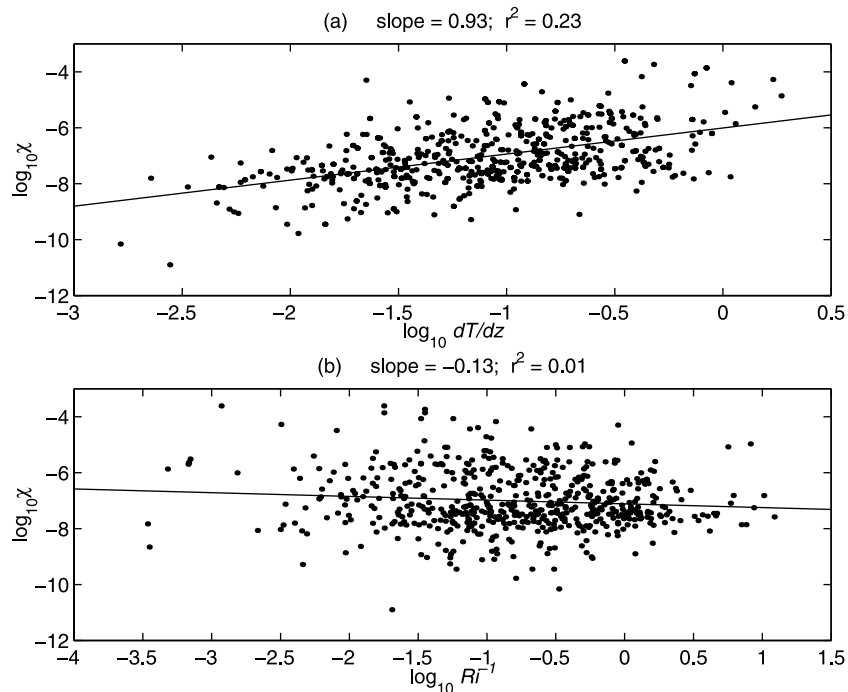
Figure 12. Dot plots of χ versus $d\bar{T}/dz$ and inverse Ri for the subset of data taken under diffusively stable conditions and having reliable, time matched mode filtered shear, N and Ri. χ shows a trend versus $d\bar{T}/dz$ but not versus Ri^{-1}. The slopes and r^2 values of the fitted lines are given. There are 587 data points.

classes (nine groups total), and no systematic variation of K resulted. The ensembles each contain too few data points to discriminate between the K values, which show no trend in any case. There are simply not enough data points from DDS conditions with good tow dynamics, reliable $d\bar{T}/dz$ and $d\bar{S}/d\bar{T}$ gradient estimates, and good ADCP/platform time registration (reliable Ri) to peform this analysis.

[38] The data can be similarly divided into ensembles of similar Ri^{-1}, irrespective of N, and K can be computed for each ensemble. Figure 13 shows that no systematic relation between K and Ri^{-1} results from this procedure.

[39] A sensible thing to do, based on the evidence of a $d\bar{T}/dz$ dependence of χ in Figure 12 and a lack of definitive relation between K and Ri^{-1}, is to compute K within ensembles containing similar $d\bar{T}/dz$ for a larger DDS data set created by easing the reliable-Ri constraint, thereby increasing the number of data points from 587 to 1904 and shrinking the confidence intervals. Figure 14 shows χ versus $d\bar{T}/dz$ for this larger data set, and also shows mean χ and mean $d\bar{T}/dz$ for five ensembles containing equal numbers of points. A power law fits the mean values fairly well. The lower part of the figure shows mean K plotted against mean $d\bar{T}/dz$, with K computed using OC from the mean $d\bar{T}/dz$ and mean χ values. The arithmetic means of χ are shown by the upper set of plotted values in each graph. Because the χ data within each ensemble have skewed distributions which are closer to lognormal than to normal, mean χ's were also computed using the maximum likelihood estimator (lnmle) of the mean of lognormal data [*Baker and Gibson*, 1987]. Mean χ and K values from this method are seen in the figure to be slightly lower than the arithmetic means and to follow the same trends. The mean χ values for

the lowest $d\bar{T}/dz$ bin appear to be overestimated by our procedures, with undue influence of high χ values at the high $d\bar{T}/dz$ end of the bin, giving rise to overestimates of K. In addition, the applicability of the OC relation is questionable for this bin containing data from very weakly stratified water, as discussed in Appendix B.

[40] The regression of logχ versus log mean $d\bar{T}/dz$ gives the relations $\chi \propto (d\bar{T}/dz)^{0.7}$ and $K \propto (d\bar{T}/dz)^{-1.3}$. If the salinity were uniform this would give $K \propto N^{-2.6}$. However, $d\bar{S}/dz$ varies systematically with $d\bar{T}/dz$ such that N^2 is proportional to $(d\bar{T}/dz)^{4/5}$ in the transect, so that the slope of -2.6 does not result if log K is plotted against log mean N for each ensemble. Figure 15 shows the result:

$$K = 10^{-10}N^{-3.3} \text{ m}^2/\text{s} \qquad (2)$$

where N is given in rad/s. This is very close to the K proportional to $N^{-3.1}$ obtained from our near-bottom data [*Rehmann and Duda*, 2000]. Note that the null result from our analysis, χ independent of $d\bar{T}/dz$, would give K proportional to N^{-5} in this figure. As in the previous figure, the highest K value may be overestimated. If that point is disregarded, the result is

$$K = 2 \times 10^{-9}N^{-2.5} \text{ m}^2/\text{s} \qquad (3)$$

with N again given in rad/s.

[41] Figure 14 shows that these data yield lower mean estimates using the lnmle method than using the arithmetic mean method, which is the opposite of what is often observed in the ocean [e.g., *Baker and Gibson*, 1987]. Figure 16 shows a probability plot of bin 3 (central) log χ data of Figure 14. Lognormally distributed data would fall
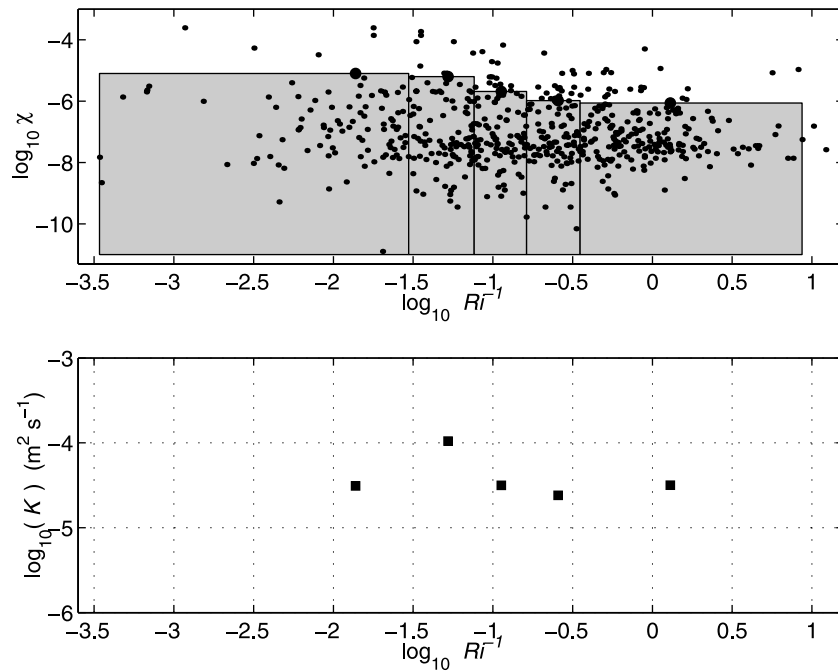
Figure 13. (top) χ is plotted versus Ri^{-1}. The 587 data points are divided into five ensembles of similar Ri^{-1}, each with comparable number of points. The widths of the shaded areas indicate the Ri^{-1} boundaries of the ensembles, and the heights indicate the mean χ within the ensembles. The mean Ri^{-1} and mean χ are indicated with symbols (asterisks within circles). (bottom) K computed for each ensemble does not show a relation to Ri^{-1}.
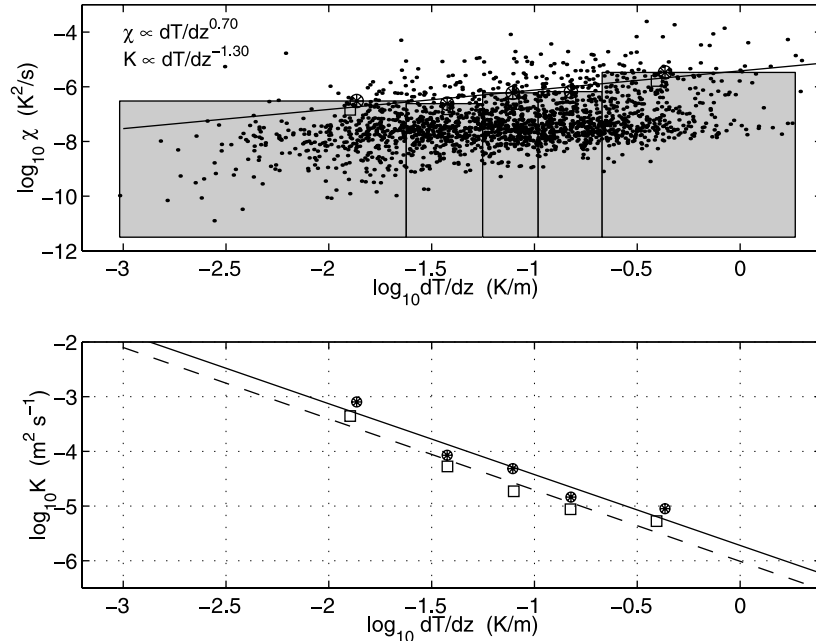

Figure 14. (top) Individual χ versus $d\bar{T}/dz$ points are shown as dots. There are 1904 data points. The arithmetic means of χ and $d\bar{T}/dz$ in five $d\bar{T}/dz$ ensembles are shown with symbols (asterisks in circles). Lognormal maximum likelihood estimate mean values are also shown (squares). The tops of the shaded boxes are aligned with the arithmetic mean values, while the widths of the boxes show the $d\bar{T}/dz$ ranges of the five ensembles. A line fitted to the arithmetic mean values is drawn, having slope 0.7 and $r^2 = 0.81$. (bottom) K resulting from the mean χ and $d\bar{T}/dz$ values obtained using the OC model are plotted versus $d\bar{T}/dz$. The upper line is the fit to the values determined from the arithmetic means in the upper frame (asterisks in circles); the lower line is the fit to Ks determined from the lnmle values of the upper frame (squares).
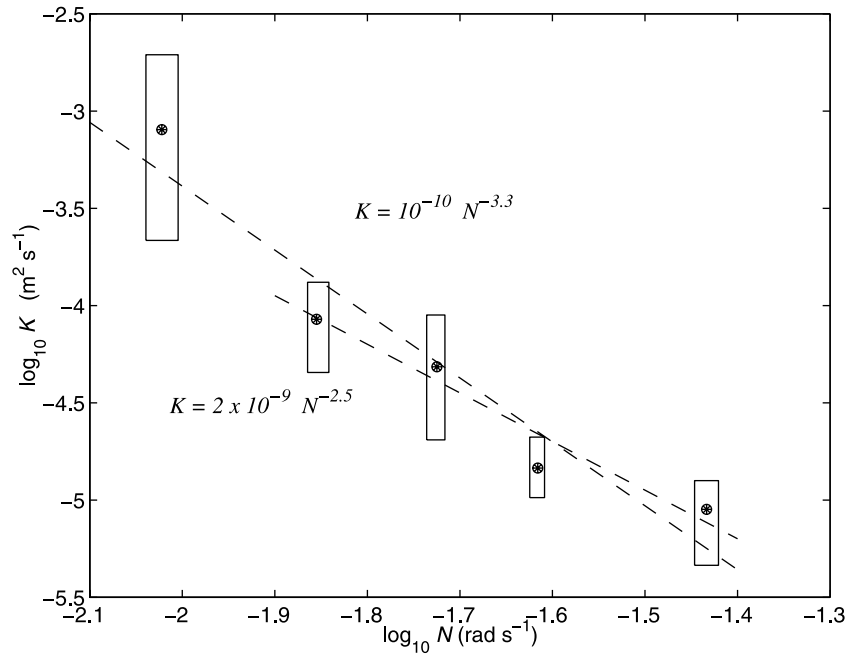
Figure 15. The arithmetic mean K values from the previous figure are plotted vs. the mean N values for each bin. The boxes outline the 95% ($2\,\sigma$) bootstrap bounds on estimates of the means of both N and K. The regression lines fit all five points or the right-hand four points, respectively.

on lines in this format. The upper 10 percent of χ values depart from the line fitting the remainder of the data. More data appear at the highest values than would appear for purely lognormal statistics. This suggests two statistical regimes and the possibility of a different physical process for the upper 10 percent than for the remainder. A candi-

date process would be intermittent very high or temporally sustained shear from internal solitary wave packets. The insufficient resolution of internal wave shear and displacement by our ADCP and tow-yo systems does not allow definitive linking of high χ events to internal solitary waves. MacKinnon and Gregg (submitted manuscript,
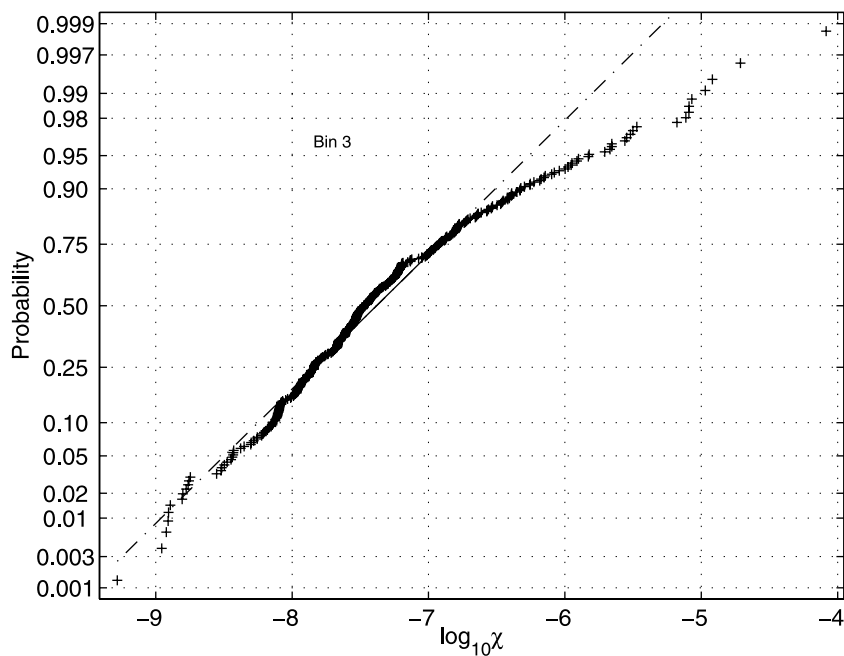
Figure 16. Bin 3 probability plot shows that χ does not behave lognormally, which is expected because the arithmetic mean estimates exceed the lnmle estimates for all bins (Figure 15). A mixture of two distributions is suggested because the upper 10–15% of data values appear to fall on a different straight line (lognormal distribution curve) than the other χ values.
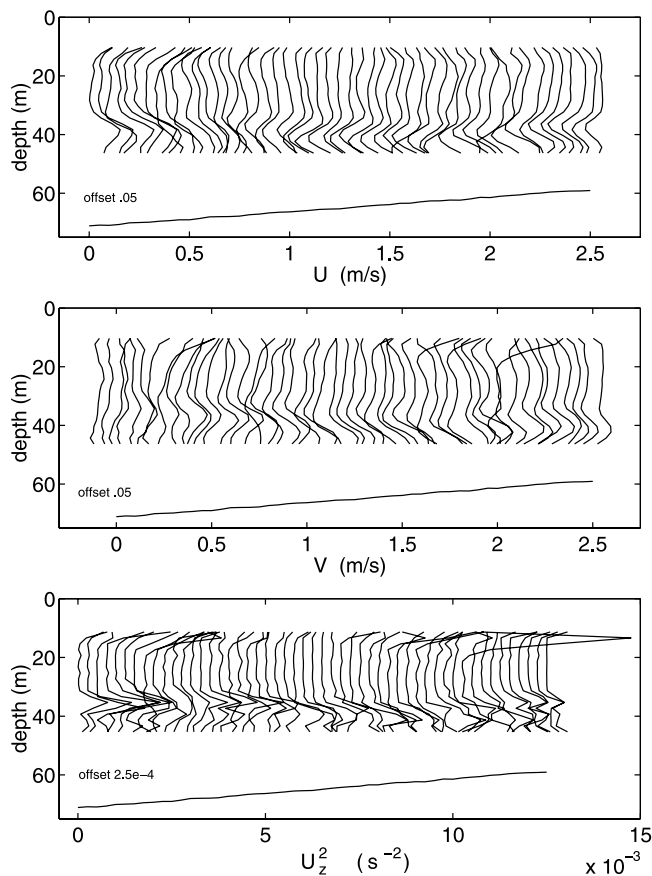
Figure 17. (top) Consecutive transect profiles of EOF-filtered U (eastward) velocity component are plotted, with each profile offset by 0.05 m/s. The depth of the seafloor is shown below each profile. (middle) The V (northward) component is plotted, similar to U above. (bottom) The squared shear $\bar{U}_z^2$ is shown similarly, offset 2.5×10^{-4} s^{-2} per profile.

2001) have observed such a connection in their CMO study.

6. Probable Cause and Implications of N-Dependent K

6.1. Discussion of the Results

[42] By subdividing the data obtained from DDS-type water according to $d\bar{T}/dz$ (roughly N) and computing statistics, we have demonstrated that K varies with buoyancy frequency according to equation (2) or (3) depending on data interpretation. Corollaries of these relations are that the buoyancy flux, given by KN^2, is proportional to $N^{-1.3}$ or $N^{-0.5}$. In this situation, diapycnal flux would be higher in less strongly stratified layers than in more strongly stratified interfaces.

[43] There is at least one very simple explanation of this behavior. If shear in the coastal ocean varies over scale longer than the scales of density fine structure, then Richardson number varies in the vertical similarly to N^2. Low Ri, with implied likelihood of shear instability, would be more likely to occur in areas of low N^2, although we would not have been able to detect U_z^2 and Ri variations at the decimeter scale with

our equipment. Continuing the argument, since shear instability drains energy from the flow field, and because a fraction of this energy (given by the mixing efficiency) is converted to potential energy via buoyancy flux, then if areas of low N lose more energy to shear instability, it is sensible for those areas to have higher buoyancy flux. The low N areas will undergo further reduction in N relative to the interfaces, sustaining the fine structure. A few studies of how a density gradient–dependent flux can create or sustain fine structure have appeared [*Pelegrí and Sangrà*, 1998; *Phillips*, 1972; *Posmentier*, 1977], and our interpretation follows hypotheses appearing in those papers. In fact, to explain the physics, it would be difficult to do better than directly quoting the entire abstract of *Phillips* [1972, p. 79]:

It is shown that if the buoyancy flux is a local property of turbulence in a stratified fluid that decreases sufficiently rapidly as the local Richardson number profile increases, than an initially linear density profile in a turbulent flow far from boundaries may become unstable with respect to small variations in the vertical density gradient. An initially linear profile will then become ragged; this possible instability may be associated on occasions with the formation of density microstructure in the ocean.

[44] It should be noted that an additional requirement for the Phillips mechanism of fine structure instability is decreasing flux as N approaches zero, which we cannot address with these data. A flattening of the K curves to less negative slope at low N (Figure 15) or low $d\bar{T}/dz$ (Figure 14) would correspond to this behavior. Such a change would result if the average χ of the left-hand bin in the top panel of Figure 14, which appears anomalously high compared to the others, were to be reduced.
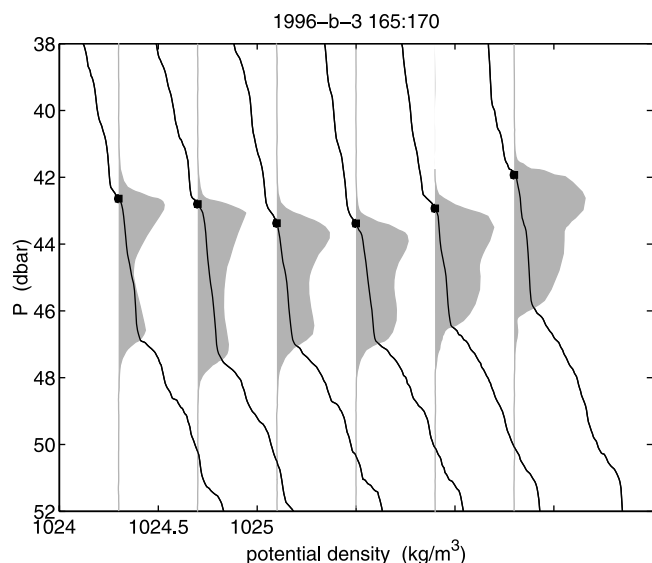
Figure 18. Six consecutive tow-yo dye and density profiles collected 100 hours after injection in DDS conditions are shown. The solid lines show the density profiles. The profiles are offset 0.4 for visual spacing. The shaded patches show the dye concentration, with the vertical left side marking zero concentration. The dye concentration scale is such that 10 ppb extends one unit on the density scale. The zero concentration baseline is placed at the x axis location of the injection target density 1024.30 and thus passes through the marked injection locations.
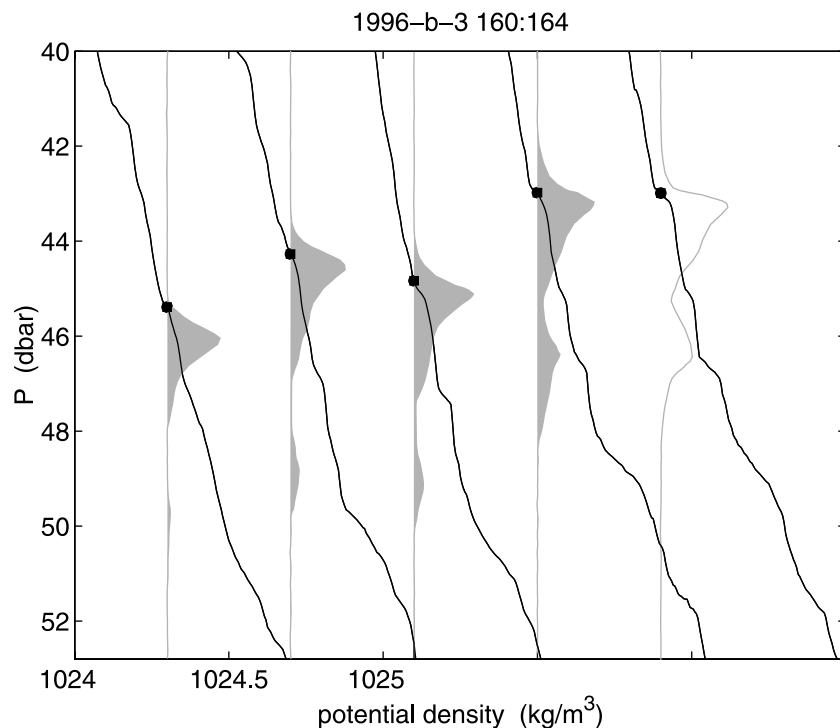
Figure 19. Five consecutive dye and density profiles are shown in the format of the previous figure. The two-lobed dye profiles may be caused by lateral migration from an area having no strong interface at these densities into this zone having the sharp density gradient between the lobes. Inhibited diffusion across the interface would prevent the lobes from connecting. The last profile shows an increased dye gradient in the high density gradient interface within the dye cloud, which would be consistent with reduced diffusivity in the interface relative to the layers above and below *and* with identical diffusive flux in both layers and the interface.

[45] Our hypothesis that shear has longer vertical scales than N cannot be addressed with our data because we can compute shear only at the relatively large 4 m scale. Figure 17 shows some shear profiles. Processes having shear at comparatively larger vertical scales include mode-one internal solitary waves, which are prevalent in the CMO area. Shear associated with these waves is evident at the upper right of the lower frame of Figure 17. We can only hypothesize that low-mode shear dominates the record, and that unresolved decimeter shear has minor effect on Ri. We can compute Ri from detailed N^2 and unresolved shear, and Ri would mimic N^2, as we hypothesize, but it would prove nothing.

[46] The buoyancy flux KN^2 from (2) will vary greatly with depth for the profiles in Figure 4. Flux proportional to $N^{-1.3}$ has a value at 25 cph which is only 12 percent of its value at 5 cph. Assuming that the mixing efficiency is the same at either stratification, a common assumption, this means that eight times more energy is dissipated at 5 cph than at 25 cph. If equal energy is put into each turbulent event, purely a hypothesis, then this is consistent with eight times as many turbulent events at 5 cph. This is not surprising, considering that Ri would be 25 times smaller at $N = 5$ cph than for $N = 25$ cph for the same shear. On the other hand, such order of magnitude variations in buoyancy flux are difficult to reconcile with the simple concept of a spatially smooth turbulent flux. An ocean with highly variable N and buoyancy flux leads to questions about effective bulk K values over scales larger than the typical

interfaces and layers. Reduced flux in the layers may control the bulk effect. This effect was investigated numerically, with results shown in the next subsection.

[47] The mean of our K estimates exceeds K measured with dye in water volumes of about 250 million cubic meters (10 by 5 km, 5 m tall) in the CMO region. If we discount our lowest $d\bar{T}/dz$ bin, which appears anomalously high in Figure 14, the remaining four K of Figure 15 average to about 4×10^{-5} m²/s. Preliminary dye release results are given by *Sundermeyer and Ledwell* [2001]; they are 0.4, 0.9, 1.5 and 3×10^{-5} m²/s. Although they do not distill their results down to a single number, MacKinnon and Gregg (submitted manuscript, 2001) observe K of 10^{-5} or less in late summer 1996 in this same area in the absence of nonlinear internal waves, and K of 40 to 100 or so times greater than that within high-shear nonlinear waves. The smaller estimates from the dye may be due to the dye reaching interfaces and stopping, and may be controlled by the reduced fluxes of the interfaces rather than the increased fluxes in low-N layers. Figures 18 and 19 show dye profiles with precisely this behavior. These profiles were collected 100 hours after the second dye injection in 1996.

6.2. Computational Diffusion Simulations

[48] In order to quantify the effective bulk diapycnal K under the circumstances of a vertically varying $K(z)$ profile (a steppy density profile under the hypothesis of N-dependent K), we have performed computational simulations of
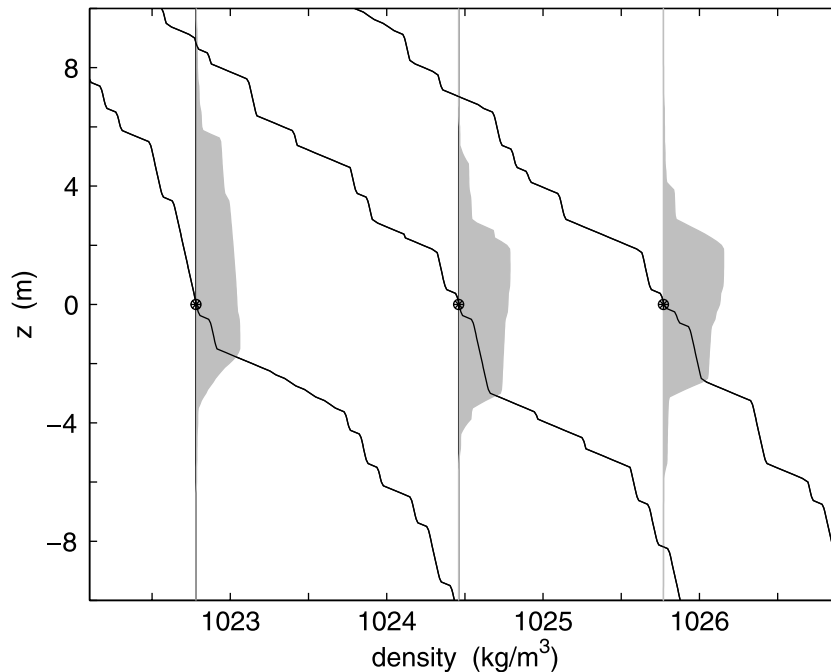
Figure 20. Simulated dye and density profiles are shown for 3 of the 50 subcloud runs of one of the 40 realizations of case 1. The formats of the dye concentration (shaded patch) and the density profiles are similar to those of Figure 18, with the density and dye profiles paired together and with the zero concentration vertical line crossing the density profile at the dye injection point. The concentration scale is arbitrary, and the sequential density profile offset is greater than Figure 18 and arbitrary because the mean density is not defined in the simulations. The three pairs of curves show completely independent structures, unlike the Figures 18 and 19, which show consecutive realizations of slowly changing ocean structure.

diffusion. These quantify the inhibiting effect of low-K layers on dispersal. We solve the one-dimensional diffusion equation for the concentration C of a passive, conservative quantity, $C_t = (KC_z)_z$, for 5 day periods in a 40 m tall vertical domain with a 0.125 m grid interval. Dye cloud dispersion experiments are simulated by summing 50 independent runs, each with unique initial conditions and fine structure. The 50 runs were intended to model different portions of an injected dye cloud (50 subclouds), each with independent fine structure and thus independent $K(z)$ structure, given by the five-point fit of Figure 15 (rule (2)). This is intended to mimic the behavior of an extended dye cloud spanning many independent regimes of ocean fine structure. This is consistent with the CMO dye experiment survey data, which showed highly variable fine structure within each dye cloud. The dye initial conditions for each of the runs are Gaussian layers with width 0.08 m, peak value 1. The positions of the 50 initial layers are taken randomly from a normal distribution such that the summed initial condition for an experiment is Gaussian with width 1 m. The fine structure for each run is created by setting $K = K_0 = 4 \times 10^{-5}$ m^2/s, equivalent to $N = 11.5$ cph by our formula. Forty-eight narrow layers of reduced K are then added, uniformly distributed in the domain, by subtracting a Gaussian function of peak value 0.97 K_0 and width 0.15 m from the background K. K is never allowed to go below a minimum K_{min} in the case of layer superposition. The resulting K profiles are skewed toward K_0, and the equivalent density profiles look quite realistic, although they

corrrespond to a slightly higher mean N (lower mean K) than conditions in four of the five CMO dye patches.

[49] Five cases were examined, with 40 realizations performed for each case. Case 1 was performed for a variable K (steppy density profile) as stated above. Case 2 was very similar, with the exception of having the 5 day dispersion interval split into two 2.5 day intervals. The first interval was performed as in case 1, except for 1/2 the time. The resulting 50 dispersed dye subclouds were then fed into new random K structure (fine structure), then diffused for an additional 2.5 days before summing to form the final dye distribution. Three additional cases were performed, each with a constant K: case 3 used the mean K from the random layer cases, 2.5×10^{-5} m^2/s; case 4 used one half that value; case 5 used one third that value.

[50] Both of the random cases make the approximation of ignoring the evolution of fine structure over time by the action of buoyancy flux divergence. The full solution requires more detailed physics and is beyond the scope of this paper [*Balmforth et al.*, 1998; *Barenblatt et al.*, 1993]. Including the physics of evolving density structure caused by N-dependent K without an additional process to erase fine structure (a process which must occur in the ocean in a manner, or over a timescale, not discernible in our data) would inhibit dye dispersal at low-K layers to even greater degree than prescribed in the simulations.

[51] Figure 20 shows concentration profiles and density profiles for three of the 50 independent subcloud runs of one case 1 realization. Concentration shows increased
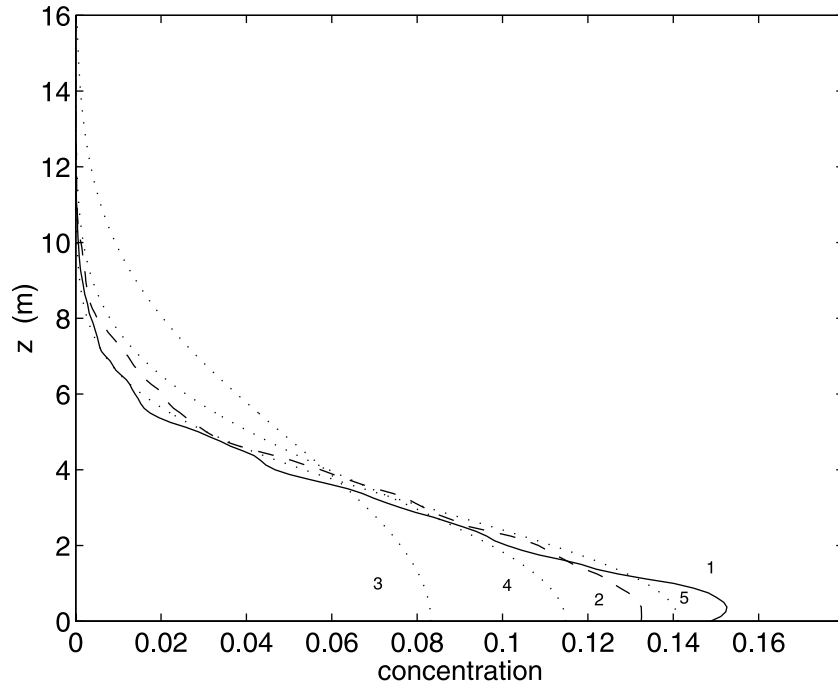
Figure 21. Dye cloud profiles are shown for one realization of each of the five dye dispersal simulation cases. The numerals 1–5 indicate the five cases. Case 1 is shown with a solid line and "1"; case 2 is shown with a dashed line and "2"; case 3 gives the largest dye spread, shown with a dotted line and "3"; case 4 is shown with a dotted line and "4"; case 5 is shown with a dotted line and "5" and is difficult to distinguish from the case 1 and case 2 curves. The lower halves of the profiles are not shown.

gradient at increased density gradient, qualitatively reproducing the behavior of dye profiles obtained from the ocean shown in the previous two figures.

[52] Figure 21 shows dye distributions from one run in each of the five cases. These are full dye cloud profiles, sums of subcloud profiles. Table 1 contains parameters and output statistics for each case. The output statistics are the vertical variance statistic $\sigma_z^2 \equiv \int C(z)(z - \bar{z})^2 dz / \int C(z) dz$ (initially one in the simulations), the patch height $4\sigma_z$, and the kurtosis or peakiness, $K_u \equiv (\sigma_z^2)^{-2} \int C(z)(z - \bar{z})^4 dz / \int C(z) dz$, with $\bar{z}$ equal to the center of mass of $C(z)$. All subcloud results in cases 3, 4, and 5 give Gaussian final concentration profiles that are symmetric about the center of the subcloud initial conditions, which sum to nearly Gaussian full cloud profiles (kurtosis of 3) in each experiment.

Cases 1 and 2 give non-Gaussian subcloud profiles that do not sum to Gaussian full cloud profiles.

[53] The results can be summarized in a few sentences. Case 1 produces non-Gaussian profiles having K_u greater than 3.4. Case 2 produces slightly wider distributions than case 1, as expected from the midterm fine-structure randomization, with σ_z^2 increased by about 10%. Case 2 profiles are closer to Gaussian than are case 1 profiles, but they are not Gaussian, with $K_u = 3.25$. Case 3, with K fixed at the mean value of case 1 and case 2 $K(z)$, gives much more dye dispersal than those cases. Cases 4 and 5, with constant K reduced from that mean K value, give dye cloud profiles which have σ_z^2 values close to the case 1 and case 2 values. Case 5 gives final full dye cloud σ_z^2 very close to case 1, and gives dye cloud profiles much like those of case 1

Table 1. Statistics From Diffusion Simulations and CMO Dye Experiments[a]

Case	K_0	K_{min}	$\bar{K}$	Intervals/Δt	$\bar{\sigma}_z^2$	$4\bar{\sigma}_z$	$\Delta\bar{\sigma}_z^2$	Mean Kurtosis
1	4	0.08	2.5	1/120	8.30/0.59	11.5	7.30	3.44 ± 0.022
2	4	0.08	2.5	2/120	9.23/0.41	12.2	8.23	3.25 ± 0.014
3	2.5	2.5	2.5	1/120	22.9/0.22	19.1	21.9	3.00 ± 0.0001
4	1.25	1.25	1.25	1/120	12.0/0.22	13.8	11.0	3.00 ± 0.0005
5	0.84	0.84	0.84	1/120	8.32/0.22	11.5	7.32	3.00 ± 0.0012
CMO-95				na/60	6.9	10.5	6.8	
CMO-96a				na/76	22.8	19.1	17.0	
CMO-96b				na/97	5.0	8.9	4.9	
CMO-97a				na/106	3.9	7.9	3.8	

[a] Dye experiment CMO-97b not included. The units of K are 10^{-5} m^2/s. Simulation intervals are defined in the text. Δt is experiment duration in hours. σ_z has units of meters. The σ_z^2 column contains mean/standard deviation of the 40 values. The RMS errors of the mean σ_z^2 estimates are always less than 0.07. $4\sigma_z$ is a characteristic patch height. $\Delta\sigma_z^2$ is the change between initial and final conditions and is proportional to K for constant K ($K = \Delta\sigma_z^2/2\Delta t$). Mean kurtosis columns contain estimated means of kurtosis values for the 40 runs of each case ± RMS error of the mean estimates.

(Figure 21), indicating that the effect of the the steppiness of the case 1 profiles is to reduce the effective K to one third of the mean K computed from the structured profiles.

[54] Preliminary scale heights of three CMO dye experiments patches, measured after 5 days, are also included in Table 1. These have been provided by J. Ledwell (personal communication, 2001). The oceanic dye experiments lasted 2.5 to 5 days, and the oceanic initial dye σ_z's for the oceanic studies were 1 m or less with the exception of CMO-96a (see table). One CMO dye experiment yielded a larger final dye patch height than our cases 1 and 2 inhomogeneous K simulations, but had interference in the dye fluorometer, two yielded smaller heights, and one yielded a comparable height.

7. Conclusion

[55] Our most detailed analysis of reliable microstructure data collected in DDS water at times when good $d\bar{T}/dz$ and $d\bar{S}/dz$ estimates were also available gives steep inverse K to N relationships, equations (2) and (3), valid for N between 0.01 and 0.05 rad/s (5.7–29 cph). One is obtained using five ensembles of data, while the other uses only four of the ensembles. These relationships are comparable to $K \propto N^{-3.1}$ observed near the bottom and reported previously [*Rehmann and Duda*, 2000]. We have assumed eddy diffusion with a defined coefficient to be an appropriate model of turbulent mixing processes occurring within spatially scattered volumes sharing common temperature and density gradient. The relationships imply that buoyancy flux KN^2 would follow $N^{-1.3}$ or $N^{-0.5}$, meaning that flux is diminished in sharper gradients, enabling the formation and sustenance of density fine struture [*Phillips*, 1972; *Posmentier*, 1977]. We have also obtained the physically similar result that K is proportional to $(d\bar{T}/dz)^{-1.3}$, with heat flux obeying $(d\bar{T}/dz)^{-0.3}$ (or a less steep relationship if the questionable data ensemble is disregarded). For comparison it should be noted that MacKinnon and Gregg (submitted manuscript, 2001) show a weak systematic relation between 4 m N^2 and K (obtained from energy dissipation) in a late summer 1996 CMO data set.

[56] An average of our K estimates of Figure 15, with the exception of the highest value, is about 4×10^{-5} m^2/s, and increases to about 9×10^{-5} if results along the fitted line are averaged. *Rehmann and Duda* [2000] reported mean K of 2 to 4×10^{-5} m^2/s for this entire transect. Computational diffusion simulations with an inhomogeneous $K(z)$ following rule (2) show that effective bulk K is about one third of the mean of $K(z)$ for those particular simulation scenarios. Table 1 shows dye dispersal through inhomogeneous $K(z)$ to be comparable to that observed in the ocean, with dye growing from 1 m to 12 m patch height in 5 days. If one accepts the hypothesis of inhomogeneous K, or, more rigorously, inhomogeneous flux, since $K(z)$ is a mathematical construct, a consistent approach would be to compare some fraction of a mean K derived from a microstructure survey to a single-valued K derived from an oceanic dye injection. *Sundermeyer and Ledwell* [2001] report 0.4, 0.9, 1.5, and 3×10^{-5} m^2/s for dye studies, whereas one third of our mean K is 0.6 to 3×10^{-5} m^2/s depending on which of the numbers mentioned in this paragraph is used, agreeing well.

[57] We have only analyzed highly resolved density fine structure and conductivity microstructure. Because our shear and Ri measurements do not have the same resolution, we can say nothing about the role of shear variability at comparable scales. Velocity typically has a red spectrum in the ocean, so we do not anticipate that current variability at these small scales plays a role, although we could not measure shear at decimeter resolution to confirm this hypothesis. The steep K versus N behavior is sensible for fields of random N and shear if shear has larger length scales than N, because small Ri would then be most common in low-N (weakly stratified) regions. Mode-one shear consistent with south New England internal solitary waves is an example of shear with larger vertical length scale than that of N, and this type of shear has been correlated with a dominant fraction of buoyancy flux in the upper half of the water column at this site (MacKinnon and Gregg, submitted manuscript, 2001).

[58] Finally, turbulent heat flux and flux divergence can be evaluated. Using K and $d\bar{T}/dz$ values from Figure 14 we can compute heat flux $F = \rho c_p K d\bar{T}/dz$, where c_p is the specific heat and ρ is the density. At $d\bar{T}/dz = 0.5°$C/m, $F = 16$ W/m^2. The heat flux at $d\bar{T}/dz = 1°$C/m, where we predict K to be 2×10^{-6} m^2/s, is reduced to 8 W/m^2, suggesting factor of two flux changes over very short vertical distances of decimeters.

Appendix A: Velocity Filtering

[59] The velocity profiles have been filtered using empirical orthogonal functions (EOF's) in an attempt to reduce the influence of noise on shear. This procedure divides the velocity record from the transect into modal constituents. The filtered record is formed by keeping low-mode signals and deleting signals from higher modes which appear to be attributable to random noise. This technique was selected over vertical filtering of individual profiles because it eliminates noise without attenuating vertically sharp features.

[60] The procedure is as follows: Complex EOFs are computed for the first and second halves of the transect, respectively. The analysis was restricted to fixed depth domains, 10 to 60 m depth in the offshore half and 10 to 46 m depth in the onshore half, so some data near the bottom were lost. This analysis decomposes the time series into orthogonal functions. The entire time series can be written as the sum of products, each product being one function and a time series of coefficients associated with that function.

[61] In each half of the record, the first seven velocity structure functions (in the vertical) were judged by their smoothness to reflect modes of oceanic velocity structure, the remainder were judged to be noise. This division of data into signal and noise assumes some coherence of the oceanic velocity structure over the duration of each subdomain. These seven functions contained 97.5 and 98.2 percent of the velocity variance, respectively. The RMS velocities of the unfiltered records were 7.9 and 9.7 cm/s, respectively. Filtered velocity data were generated by summing only the first seven EOF/coefficient products. These exhibited areas of very low shear, areas with persistently high shear, and transient effects of small-scale nonlinear

internal waves, Figure 17. The RMS values of the deleted velocities, judged to be noise, were 1.2 and 1.0 cm/s, respectively, consistent with accepted estimates of ADCP noise. The filtered velocity series are first differenced to obtain squared shear, Figure 17. The resulting shears are merged with filtered tow platform data to give Ri using the matching procedure described in section 4. The filtering process removes about 50% of the shear variance, presumably due to noise, which increases Ri values accordingly. The procedure removes only about 2% percent of the velocity variance, retains vertical detail, and retains temporal (along-track) structures.

Appendix B: Application of the Osborn-Cox Model

[62] We depend on a balance of two terms in equation (1), the balance of *Osborn and Cox* [1972], for our major results. The results (equations (2) and (3)) are obtained over five and four ensembles, respectively, and accuracy of those relationships between K and N depends upon any bias being equal in the ensembles (preferably zero). The relationships between K and N and between flux and N ultimately depend on the observed relationship between χ and $d\bar{T}/dz$ and the applicability of the OC model. Improper disregard of the other terms can manifest itself in the results in at least two ways: (1) The neglected terms can be significant in all ensembles, with (approximately) equal scaling in all ensembles, leading to an (approximately) equal positive multiplicative bias of K in each ensemble; (2) The scaling of the terms in equation (1) may vary over ensemble, with unequal error or bias of K in the ensembles. An example of type 2 would be an advection of variance into low-N layers from adjoining high-N interfaces. Such a systematic unidirectional "dragging" of thermal fluctuations from the interfaces into the layers, which must eventually dissipate, might lead to the observed systematic relation between χ and $d\bar{T}/dz$, Figure 14 (basically between χ and N).

[63] The temporal variation term in equation (1) has been eliminated on the grounds that the hundreds of points in each ensemble sample the population of developing to decaying turbulence in an unbiased fashion. The triple-correlation flux divergence term has been eliminated on the basis of an argument give by *Washburn* [1987]. In that paper, a method for estimating the rms inward velocity (u) required for the flux divergence term to approach dissipation within a two-dimensional depth- and laterally bounded region using Gauss' theorem is presented, yielding $u_{rms} = (\chi H)/(c_2((T')^2)_{rms})$, where c_2 is a correlation coefficient between normal velocity component and $(T')^2$ fluctuation and where H is height. Repeating that analysis for regions having 4 m tall ($H = 2$) trial geometry, meant to represent relatively well-mixed layers bounded above and below by interfaces, the result is that continuously acting spatially uniform $u_{rms} = 1$ mm/s across the boundaries under conditions of perfectly correlated $(T')^2$ and u variations (i.e., $c_2 = -1$) would supply the variance needed to balance χ of 10^{-6} K²/s, where our observed $((T')^2)_{rms} = 2 \times 10^{-3}$ °C² has been used. We judge the correlation and the spatial uniformity to be improbable, and suggest that higher turbulent velocities would be required to transport variance, perhaps by a factor of three to account for decorrelation and a factor of 20 to account for the fact that mixing activity

will be absent at much of the boundary, giving a required diapycnal velocity of 6 cm/s in patches. Assuming isotropy and some decorrelation, dividing the time averaged turbulent energy $3(0.5(0.003)^2)$ m²/s² by the mean dissipation estimate of $\epsilon = 10^{-8}$ W/kg for the region (MacKinnon and Gregg, submitted manuscript, 2001) gives a 20 minute timescale for the turbulent energy. This is many times N^{-1}, so the actual velocities may be less, making the flux divergence negligible and enabling the OC balance. Ozmidov scaling of velocity also provides an expected u, $u_o = (\epsilon/N)^{1/2}$; use of the same ϵ and the value $N = 15$ cph gives $u_o = 0.0006$ m/s, small enough to defend elimination of the flux divergence term.

[64] The OC relation yields a very high K in the least stratified ensemble. The limiting case of a weakly stratified layer bounded by sharp interfaces, which would be in that ensemble, is most troublesome with respect to the flux divergence term, despite the arguments of the previous paragraphs defending its elimination. It is not unreasonable to hypothesize that temperature variance would be larger in the high-N interfaces above and below the low-N box, and that exchange between the layers and interfaces would preferentially bring thermal variance into the box. In this situation, particularly if $d\bar{T}/dz$ were near zero, the production term in the budget equation (1) may not balance χ as in the OC model, although we defend this balance in the previous paragraph. Instead, time dependence or transport from the bounding layers may play a role. Assuming that flux in the layer can still be described by Fick's law, this leads to an alternative to the OC relation

$$K = \frac{\chi - A}{2(d\bar{T}/dz)^2}$$

where A is the sum of the first two terms of equation (1). In this case OC would overestimate K. This may be a possibility for the left-hand one or two bins of the lower panel of Figure 14 and of Figure 15. There are at least three possibilities for the low-N layers: (1) OC applies and local K in the layers has been correctly estimated. (2) OC is slightly inaccurate and K is slightly overestimated, but mixing in the layers is strong enough that the entrained density anomalies eventually dissipate; (3) OC does not apply because variance flux divergence (neglected by OC) is large, so use of OC overestimates K in the layers. In case 3, entrainment of density anomalies by the same process which entrains variance preferentially into layers might cause the layers to stratify (i.e., disappear), so case 3 seems inconsistent with the existence of the fine structure, but is nonetheless possible.

[65] The OC relation and its alternative discussed above are built upon χ estimates. Whereas χ is the sum of gradient variance in three dimensions, we have only measured gradient variance along a one-dimensional track and multiplied by three to account for variance in the normal directions, thus assuming isotropic statistics (see section 2). This procedure may equally bias all of the values in the top panel of Figure 14, thus biasing the fitted lines upward or downward but not changing their slopes. On the other hand, variable levels of anisotropy in the ensembles would give unequal biases in the bins and would introduce slope errors. One might expect a low bias for χ estimated from a gradient

normal component using the isotropy assumption [see *Rehmann and Duda*, 2000, section 4b].

References

Baker, M. A., and C. H. Gibson, Sampling turbulence in the stratified ocean: Statistical consequences of strong intermittency, *J. Phys. Oceanogr.*, *17*, 1817–1836, 1987.

Balmforth, N. J., S. G. Llewellyn Smith, and W. R. Young, Dynamics of interfaces and layers in a stratified turbulent fluid, *J. Fluid Mech.*, *355*, 329–358, 1998.

Barenblatt, G. I., M. Bertsch, R. D. Passo, V. M. Protokishin, and M. Ughi, A mathematical model of turbulent heat and mass transfer in stably stratified shear flow, *J. Fluid Mech.*, *253*, 341–358, 1993.

Davis, R. E., Diapycnal mixing in the ocean: The Osborn-Cox model, *J. Phys. Oceanogr.*, *24*, 2560–2576, 1994.

Donaghay, P. L., H. M. Rines, and J. M. Sieburth, Advanced techniques for in situ studies of zooplankton abundance, distribution, and behavior, *Adv. Limnol.*, *36*, 97–108, 1992.

Gardner, W. D., et al., Optics, particles, stratification and storms on the New England continental shelf, *J. Geophys. Res.*, *106*, 9473–9497, 2001.

Gregg, M. C., and T. B. Sanford, The dependence of turbulent dissipation on stratification in a diffusively stable thermocline, *J. Geophys. Res.*, *93*, 12,381–12,392, 1988.

Meagher, T. B., A. M. Pederson, and M. C. Gregg, A low-noise conductivity microstructure instrument, in *Proceedings of Oceans '82*, 283–290, Inst. of Electr. and Electr., Eng., New York, 1982.

Mellor, G. L., and T. Yamada, Development of a turbulence closure model for geophysical fluid problems, *Rev. Geophys.*, *20*, 851–875, 1982.

Moody, J. A., et al., Atlas of tidal elevations and current observations on the northeast American Continental Shelf and Slope, *U.S. Geol. Surv. Bull.*, *1611*, 122 pp., 1984.

Nash, J. D., and J. N. Moum, Estimating salinity variance dissipation rate from conductivity microstructure measurements, *J. Atmos. Ocean. Technol.*, *16*, 263–274, 1999.

Osborn, T. R., and C. S. Cox, Oceanic fine structure, *Geophys. Fluid Dyn.*, *3*, 321–345, 1972.

Pacanowski, R. C., and S. G. H. Philander, Parameterization of vertical mixing in numerical models of tropical oceans, *J. Phys. Oceanogr.*, *11*, 1443–1451, 1981.

Pelegrí, J. L., and P. Sangrà, A mechanism for layer formation in stratified geophysical flows, *J. Geophys. Res.*, *103*, 30,679–30,693, 1998.

Phillips, O. M., Turbulence in a strongly stratified fluid—Is it unstable?, *Deep Sea Res.*, *19*, 79–81, 1972.

Posmentier, E. S., The generation of salinity finestructure by vertical diffusion, *J. Phys. Oceanogr.*, *7*, 298–300, 1977.

Rehmann, C. R., and T. F. Duda, Diapycnal diffusivity inferred from scalar microstructure measurements near the New England shelf/slope front, *J. Phys. Oceanogr.*, *30*, 1354–1371, 2000.

Smyth, W. D., J. N. Moum, and D. R. Caldwell, The efficiency of mixing in turbulent patches: Inferences from direct simulations and microstructure observations, *J. Phys. Oceanogr.*, *31*, 1969–1992, 2001.

St. Laurent, L., and R. W. Schmitt, The contribution of salt fingers to vertical mixing in the North Atlantic Tracer Release Experiment, *J. Phys. Oceanogr.*, *29*, 1404–1424, 1999.

Sundermeyer, M. A., and J. R. Ledwell, Lateral dispersion over the continental shelf: Analysis of dye-release experiments, *J. Geophys. Res.*, *106*, 9603–9621, 2001.

Turner, J. S., *Buoyancy Effects in Fluids*, Cambridge Univ. Press, New York, 1973.

Washburn, L., Two-dimensional observations of temperature microstructure in a coastal region, *J. Geophys Res.*, *92*, 10,787–10,798, 1987.

Washburn, L., T. F. Duda, and D. C. Jacobs, Interpreting conductivity microstructure: Estimating the temperature variance dissipation rate, *J. Atmos. Oceanic Technol.*, *13*, 1166–1188, 1996.

———————

T. F. Duda, AOPE Department, MS 11, Woods Hole Oceanographic Institution, Woods Hole, MA 02543, USA. (tduda@whoi.edu)

C. R. Rehmann, Department of Civil and Environmental Engineering, University of Illinois at Urbana-Champaign, Urbana, IL 61801, USA.